

Probing spin hydrodynamics on a superconducting quantum simulator

Yun-Hao Shi,^{1,2,3,*} Zheng-Hang Sun,^{1,2,*} Yong-Yi Wang,^{1,2,*} Zheng-An Wang,^{3,4} Yu-Ran Zhang,⁵ Wei-Guo Ma,^{1,2} Hao-Tian Liu,^{1,2} Kui Zhao,³ Jia-Cheng Song,^{1,2} Gui-Han Liang,^{1,2} Zheng-Yang Mei,^{1,2} Jia-Chi Zhang,^{1,2} Hao Li,¹ Chi-Tong Chen,^{1,2} Xiaohui Song,¹ Jieci Wang,⁶ Guangming Xue,³ Haifeng Yu,³ Kaixuan Huang,^{3,†} Zhongcheng Xiang,^{1,2,‡} Kai Xu,^{1,2,3,4,7,8,§} Dongning Zheng,^{1,2,4,7,8} and Heng Fan^{1,2,3,4,7,8,¶}

¹*Institute of Physics, Chinese Academy of Sciences, Beijing 100190, China*

²*School of Physical Sciences, University of Chinese Academy of Sciences, Beijing 100049, China*

³*Beijing Academy of Quantum Information Sciences, Beijing 100193, China*

⁴*Hefei National Laboratory, Hefei 230088, China*

⁵*School of Physics and Optoelectronics, South China University of Technology, Guangzhou 510640, China*

⁶*Department of Physics and Key Laboratory of Low Dimensional Quantum Structures and Quantum Control of Ministry of Education, Hunan Normal University, Changsha, Hunan 410081, China*

⁷*Songshan Lake Materials Laboratory, Dongguan, Guangdong 523808, China*

⁸*CAS Center for Excellence in Topological Quantum Computation, UCAS, Beijing 100190, China*

Characterizing the nature of hydrodynamical transport properties in quantum dynamics provides valuable insights into the fundamental understanding of exotic non-equilibrium phases of matter. Simulating infinite-temperature transport on large-scale complex quantum systems remains an outstanding challenge. Here, using a controllable and coherent superconducting quantum simulator, we experimentally realize the analog quantum circuit, which can efficiently prepare the Haar-random states, and probe spin transport at infinite temperature. We observe diffusive spin transport during the unitary evolution of the ladder-type quantum simulator with ergodic dynamics. Moreover, we explore the transport properties of the systems subjected to strong disorder or a tiled potential, revealing signatures of anomalous subdiffusion in accompany with the breakdown of thermalization. Our work demonstrates a scalable method of probing infinite-temperature spin transport on analog quantum simulators, which paves the way to study other intriguing out-of-equilibrium phenomena from the perspective of transport.

Transport properties of quantum many-body systems driven out of equilibrium are of significant interest in several active areas of modern physics, including the ergodicity of quantum systems [1–4] and quantum magnetism [5–7]. Understanding these properties is crucial to unveil the non-equilibrium dynamics of isolated quantum systems [8, 9]. One essential property of transport is the emergence of classical hydrodynamics in microscopic quantum dynamics, which shows the power-law tail of autocorrelation functions [8]. The rate of the power-law decay, referred as to the transport exponent, characterizes the universal classes of hydrodynamics. In d -dimensional quantum systems, in addition to generally expected diffusive transport with the exponent $d/2$ in non-integrable systems [10–12], more attentions have been attracted by the anomalous superdiffusive [5, 13–16] or subdiffusive transport [2, 3, 17–19], with the exponent larger or smaller than $d/2$, respectively.

Over the last few decades, considerable strides have

been made in enhancing the scalability, controllability, and coherence of noisy intermediate-scale quantum (NISQ) devices based on superconducting qubits. With these advancements, several novel phenomena in non-equilibrium dynamics of quantum many-body systems have been observed, such as quantum thermalization [20, 21], ergodicity breaking [22–25], time crystal [26–28], and information scrambling [29, 30]. More importantly, in this platform, the quantum advantage has been demonstrated by sampling the final Haar-random states of randomized sequences of gate operations [31–35]. Recently, a method of measuring autocorrelation functions at infinite temperature based on the Haar-random states has been proposed, which opens up a practical application of pseudo-random quantum circuits for simulating hydrodynamics on NISQ devices [36, 37].

In this work, using a ladder-type superconducting quantum simulator with up to 24 qubits, we first demonstrate that in addition to the digital pseudo-random circuits [31–37], a unitary evolution governed by a time-independent Hamiltonian, i.e., an analog quantum circuit, can also build up the necessary randomness for measuring the infinite-temperature autocorrelation functions [38]. Subsequently, we study the properties of spin transport on the superconducting quantum simulator via the measurement of autocorrelation functions by using

* These authors contributed equally to this work.

† huangkx@baqis.ac.cn

‡ zcxiang@iphy.ac.cn

§ kaixu@iphy.ac.cn

¶ hfan@iphy.ac.cn

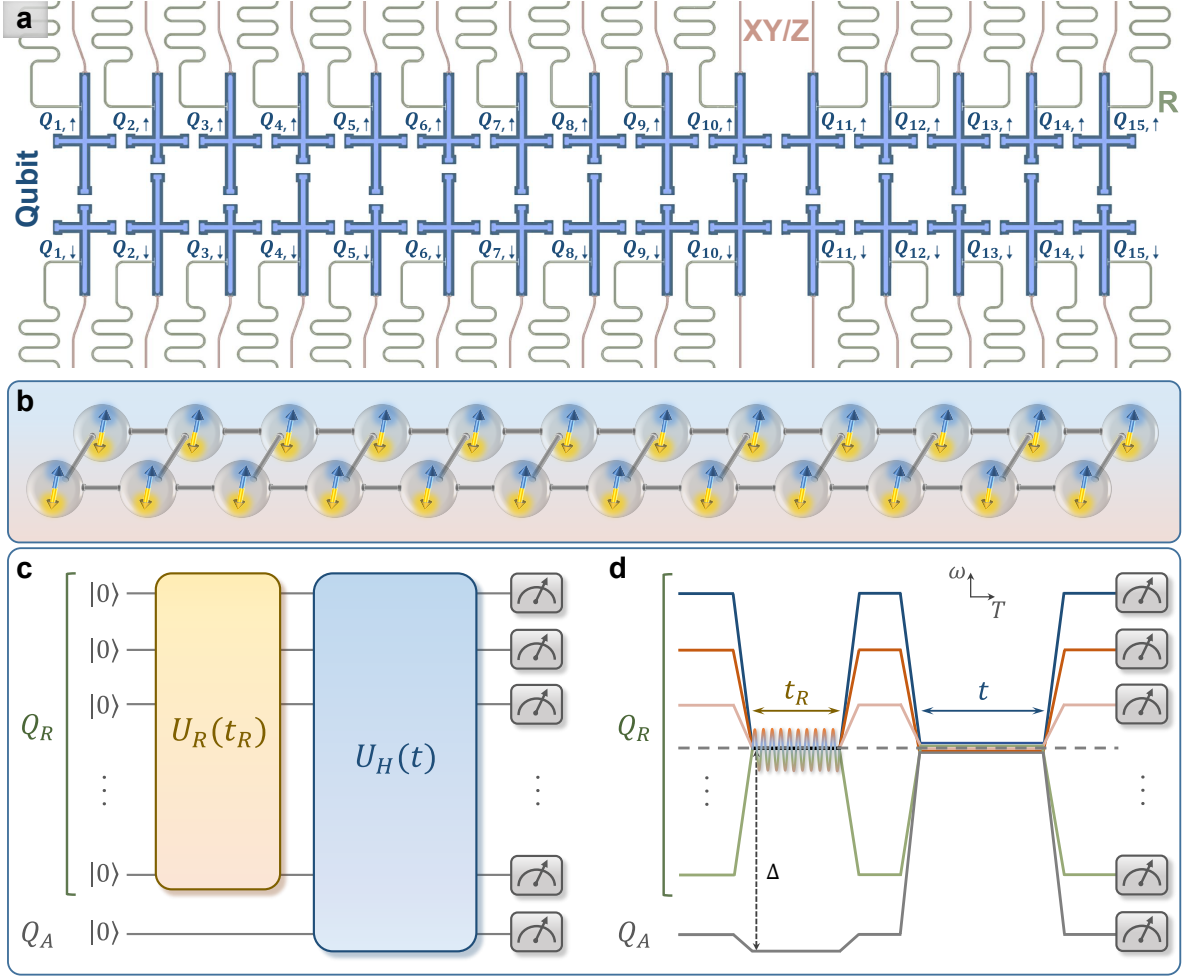


FIG. 1. **Superconducting quantum simulator and experimental pulse sequences.** **a**, The optical micrograph showing the ladder-type superconducting quantum simulator, consisting of 30 qubits (the blue region), labeled $Q_{1,\uparrow}$ to $Q_{15,\uparrow}$ and $Q_{1,\downarrow}$ to $Q_{15,\downarrow}$. Each qubit is coupled to a separate readout resonator (the green region), and has an individual control line (the red region) for both the XY and Z controls. **b**, Schematic diagram of the simulated 24 spins coupled in a ladder. The blue and yellow double arrows represent the infinite-temperature spin hydrodynamics without preference for spin orientations. **c**, Schematic diagram of the quantum circuit for measuring the autocorrelation functions at infinite temperature. All qubits are initialized at the state $|0\rangle$. Subsequently, a pseudo-random circuit $\hat{U}_R(t_R)$ acts on the set of qubits Q_R . This is followed by a time evolution of all qubits, i.e., $\hat{U}_H(t) = \exp(-i\hat{H}t)$ with \hat{H} being the Hamiltonian of the system, in which the properties of spin transport are of our interest. **d**, Experimental pulse sequences corresponding to the quantum circuit in **c**, displayed in the frequency (ω) versus time (T) domain. To realize $\hat{U}_R(t_R)$, qubits in the set Q_R are tuned to the working point (dashed horizontal line) via Z pulses, and simultaneously, the resonant microwave pulses represented as the sinusoidal line are applied to Q_R through the XY control lines. Meanwhile, the qubit Q_A is detuned from the working point with a large value of the frequency gap Δ . To realize the subsequent evolution $\hat{U}_H(t)$ with the Hamiltonian (1), all qubits are tuned to the working point.

the Haar-random states. Notably, we observe a clear signature of the diffusive transport on the qubit ladder, which is a non-integrable system [11, 12].

Upon subjecting the qubit ladder to disorder, a transition from delocalized phases to the many-body localization (MBL) occurs as the strength of disorder in-

creases [39]. By measuring the autocorrelation functions, we experimentally probe an anomalous subdiffusive transport with intermediate values of the disorder strength. The observed signs of subdiffusion are consistent with recent numerical results, and can be explained as a consequence of Griffith-like region on the delocalized

side of the MBL transition [2, 3, 40–43].

Finally, we explore spin transport on the qubit ladder with a linear potential, and it is expected that Stark MBL occurs when the potential gradients are sufficiently large [24, 44–48]. With a large gradient, the conservation of the dipole moment emerges [24, 48], associated with the phenomena known as the Hilbert space fragmentation [49–51]. Recent theoretical works reveal a subdiffusion in the dipole-moment conserving systems [17, 19]. In this experiment, we present evidence of a subdiffusive regime of spin transport in the titled qubit ladder.

Experimental setup and protocol

Our experiments are performed on a programmable superconducting quantum simulator, consisting of 30 transmon qubits with a geometry of two-legged ladder, see Fig. 1a and b. The nearest-neighbor qubits are coupled by a fixed capacitor, and the effective Hamiltonian of capacitive interactions can be written as [52, 53] (also see Supplementary Section I)

$$\begin{aligned} \hat{H}_I/\hbar = & \sum_{m \in \{\uparrow, \downarrow\}} \sum_{j=1}^{L-1} J_{j,m}^{\parallel} (\hat{\sigma}_{j,m}^+ \hat{\sigma}_{j+1,m}^- + \text{H.c.}) \\ & + \sum_{j=1}^L J_j^{\perp} (\hat{\sigma}_{j,\uparrow}^+ \hat{\sigma}_{j,\downarrow}^- + \text{H.c.}), \end{aligned} \quad (1)$$

where $\hbar = h/2\pi$, with h being the Planck constant (in the following we set $\hbar = 1$), L is the length of the ladder, $\hat{\sigma}_{j,m}^+$ ($\hat{\sigma}_{j,m}^-$) is the raising (lowering) operator for the qubit $Q_{j,m}$, and $J_{j,m}^{\parallel}$ (J_j^{\perp}) refers to the rung (intrachain) hopping strength. The XY and Z control lines on the device enable us to realize the drive Hamiltonian $\hat{H}_d = \sum_{m \in \{\uparrow, \downarrow\}} \sum_{j=1}^L \Omega_{j,m} (e^{-i\phi_{j,m}} \hat{\sigma}_{j,m}^+ + e^{i\phi_{j,m}} \hat{\sigma}_{j,m}^-)/2$, and the on-site potential Hamiltonian $\hat{H}_Z = \sum_{m \in \{\uparrow, \downarrow\}} \sum_{j=1}^L w_{j,m} \hat{\sigma}_{j,m}^+ \hat{\sigma}_{j,m}^-$, respectively. Here, $\Omega_{j,m}$ and $\phi_{j,m}$ denote the driving amplitude and the phase of the microwave pulse applied on the qubit $Q_{j,m}$, and $w_{j,m}$ is the effective on-site potential.

To study spin transport and hydrodynamics, we focus on the equal-site autocorrelation function at infinite-temperature, which is defined as

$$C_{\mathbf{r},\mathbf{r}} = \frac{1}{D} \text{Tr}[\hat{\rho}_{\mathbf{r}}(t) \hat{\rho}_{\mathbf{r}}], \quad (2)$$

where $\hat{\rho}_{\mathbf{r}}$ is a local observable at site \mathbf{r} , $\hat{\rho}_{\mathbf{r}}(t) = e^{i\hat{H}t} \hat{\rho}_{\mathbf{r}} e^{-i\hat{H}t}$, and D is the Hilbert dimension of the Hamiltonian \hat{H} . Here, for the ladder-type superconducting simulator, we choose $\hat{\rho}_{\mathbf{r}} = (\hat{\sigma}_{1,\uparrow}^z + \hat{\sigma}_{1,\downarrow}^z)/2$ ($\mathbf{r} = 1$) [12], and the autocorrelation function can be rewritten as

$$C_{1,1} = \frac{1}{4} (c_{1,\uparrow;1,\uparrow} + c_{1,\uparrow;1,\downarrow} + c_{1,\downarrow;1,\uparrow} + c_{1,\downarrow;1,\downarrow}), \quad (3)$$

with $c_{\alpha;\beta} = \text{Tr}[\hat{\sigma}_{\alpha}^z(t) \hat{\sigma}_{\beta}^z]/D$ (subscripts α and β denote the qubit index 1, \uparrow or 1, \downarrow).

The autocorrelation functions (2) at infinite temperature can be expanded as the average of $C_{\mathbf{r},\mathbf{r}}(|\psi_0\rangle) = \langle \psi_0 | \hat{\rho}_{\mathbf{r}}(t) \hat{\rho}_{\mathbf{r}} | \psi_0 \rangle$ over different $|\psi_0\rangle$ in z -basis. In fact, the dynamical behavior of an individual $C_{\mathbf{r},\mathbf{r}}(|\psi_0\rangle)$ is sensitive to the choice of $|\psi_0\rangle$ under some circumstances (see Supplementary Section VII for the dependence of $C_{\mathbf{r},\mathbf{r}}(|\psi_0\rangle)$ on $|\psi_0\rangle$ in the qubit ladder with a linear potential as an example). To experimentally probe the generic properties of spin transport at infinite temperature, one can obtain (2) by measuring and averaging $C_{\mathbf{r},\mathbf{r}}(|\psi_0\rangle)$ with different $|\psi_0\rangle$ [15]. Alternatively, we employ a more efficient method to measure (2) without the need of sampling different $|\psi_0\rangle$. Based on the results in ref. [36] (also see Methods), the autocorrelation function $c_{\alpha;\beta}$ can be indirectly measured by using the quantum circuit as shown in Fig. 1c, i.e.,

$$c_{\alpha;\beta} \simeq \langle \psi_{\beta}^R(t) | \hat{\sigma}_{\alpha}^z | \psi_{\beta}^R(t) \rangle, \quad (4)$$

where $|\psi_{\beta}^R(t)\rangle = \hat{U}_H(t)[|0\rangle_{\beta} \otimes |\psi^R\rangle]$ with $|\psi^R\rangle = \hat{U}_R(t_R) \otimes_{i \in Q_R} |0\rangle_i$. For example, to experimentally obtain $c_{1,\downarrow;1,\uparrow}$, we choose $Q_{1,\uparrow}$ as Q_A , and the remainder qubits as the Q_R . After performing the pulse sequences as shown in Fig. 1d, we measure the qubit $Q_{1,\downarrow}$ at z -basis to obtain the expectation value of the observable $\hat{\sigma}_{1,\downarrow}^z$.

Observation of diffusive transport

In this experiment, we first study spin transport on the 24-qubit ladder consisting of $Q_{1,\uparrow}, \dots, Q_{12,\uparrow}$ and $Q_{1,\downarrow}, \dots, Q_{12,\downarrow}$, described by the Hamiltonian (1). For a non-integrable model, one expects that diffusive transport $C_{1,1} \propto t^{-1/2}$ occurs [12]. To measure the autocorrelation function $C_{1,1}$ defined in Eq. (3), pseudo-random quantum circuits should be performed to generate the required Haar-random states $|\psi^R\rangle$. Instead of using the digital random circuits in refs. [31–37], here we experimentally realize the time evolution under the Hamiltonian $\hat{H}_R = \hat{H}_I + \hat{H}_d$, where the parameters $\Omega_{j,m}$ and $\phi_{j,m}$ in \hat{H}_d have site-dependent random values (see Methods), i.e., $\hat{U}_R(t_R) = \exp(-i\hat{H}_R t_R)$, which is more suitable for our analog quantum simulator. To benchmark that the final state $|\psi^R\rangle = \hat{U}_R(t_R)|0\rangle$ can approximate the Haar-random states, we measure the participate entropy $S_{\text{PE}} = -\sum_{k=1}^D p_k \ln p_k$, with $p_k = |\langle k | \psi^R \rangle|^2$ and $\{|k\rangle\}$ being a computational basis. Figure 2a shows the results of S_{PE} with different evolution times t_R . For the 23-qubit system, the probabilities p_k are estimated from the single-shot readout with a number of samples $N_s = 3 \times 10^7$. It is seen that the S_{PE} tends to the pseudo-random value $S_{\text{PE}}^T = N \ln 2 - 1 + \gamma$ with $N = 23$ being the number of qubits and $\gamma \simeq 0.577$ as the Euler's constant [32]. Moreover, for the final state $|\psi^R\rangle$ with

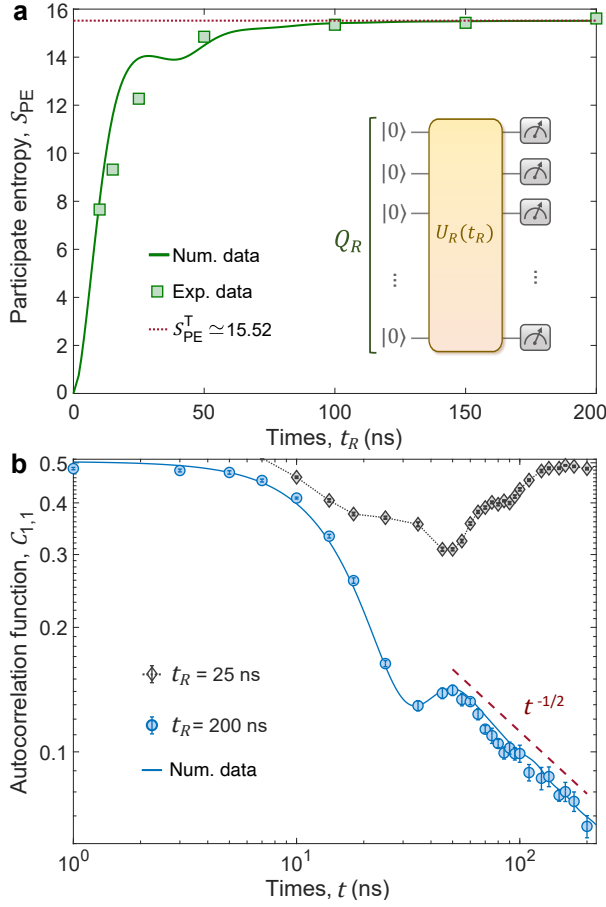


FIG. 2. **Observation of diffusive transport.** **a**, Experimental verification of preparing the states via the time evolution of participate entropy. Here, we chose $Q_R = \{Q_{1,\uparrow}, Q_{2,\uparrow}, \dots, Q_{12,\uparrow}, Q_{2,\downarrow}, Q_{3,\downarrow}, \dots, Q_{12,\downarrow}\}$ with total 23 qubits. The inset of **a** shows the corresponding quantum circuit. The dotted horizontal line represents the pseudo-random value of participate entropy, i.e., $S_{PE}^T \approx 15.519$. **b**, Experimental results of the autocorrelation function $C_{1,1}(t)$ for the qubit ladder with $L = 12$, which are measured by performing the quantum circuit shown in Fig. 1c and d. Here, we consider two different states generated from $\hat{U}_R(t_R)$ with $t_R = 25$ ns and 200 ns. Markers are experimental data. The solid line is the numerical simulation of the correlation function $C_{1,1}$ at infinite temperature. The dashed line represents a power-law decay $t^{-1/2}$. Error bars represent the standard deviation.

$t_R = 200$ ns, the distribution of probabilities p_k satisfies the Porter-Thomas distribution (see Supplementary Section VI).

In Fig. 2b, we show the dynamics of the autocorrelation function $C_{1,1}$ measured via the quantum circuit in Fig. 1c with $t_R = 200$ ns. The experimental data satisfies $C_{1,1} \propto t^{-z}$, with a transport exponent $z \approx 0.5067$, estimated by fitting the data in the time window $t \in$

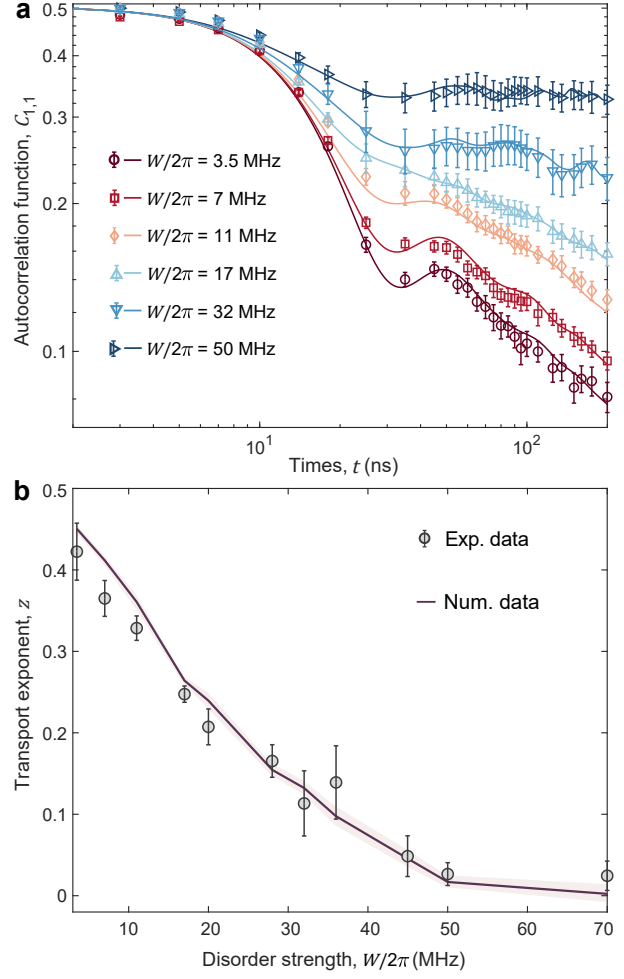


FIG. 3. **Subdiffusive transport on the superconducting qubit ladder with disorder.** **a**, The time evolution of autocorrelation function $C_{1,1}(t)$ for the qubit ladder with $L = 12$ and different values of disorder strength W . Markers (lines) are experimental (numerical) data. **b**, Transport exponent z as a function of W obtained from fitting the data of $C_{1,1}(t)$. Error bars (experimental data) and shaded regions (numerical data) represent the standard deviation.

[50 ns, 200 ns]. In contrast, with $t_R = 25$ ns, the state $|\psi^R\rangle$ does not approach to the Haar-random states, and its value of S_{PE} is much smaller than the S_{PE}^T (Fig. 2a). By employing the state $|\psi^R\rangle$ with $t_R = 25$ ns, the values of the observable defined in Eq. (4) is incompatible with diffusive transport (Fig. 2b). Our experiments clearly show that spin diffusively transports on the qubit ladder \hat{H}_I (1), and demonstrate that the analog pseudo-random quantum circuit $\hat{U}_R(t_R)$ with $t_R = 200$ ns can provide sufficient randomness to measure the autocorrelation function defined in Eq. (2) and probe infinite-temperature spin transport. In the following, we fix $t_R = 200$ ns, and study spin

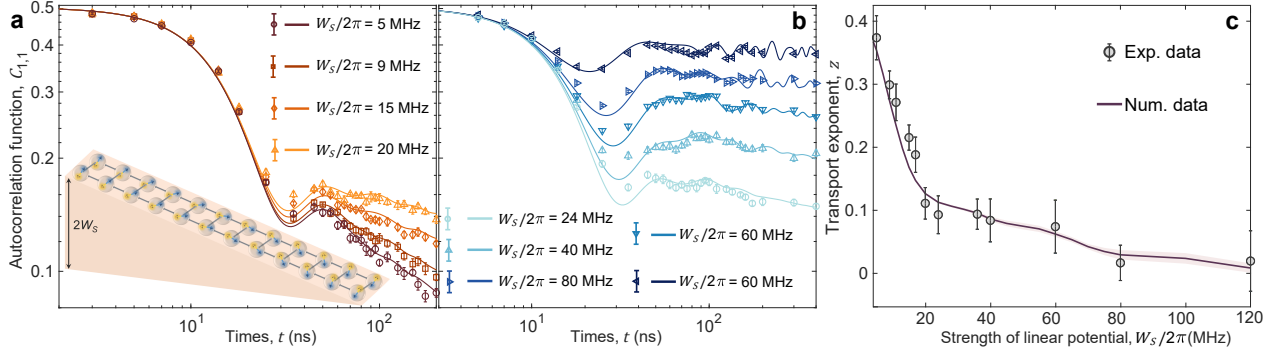


FIG. 4. **Subdiffusive transport on the superconducting qubit ladder with linear potential.** **a**, Time evolution of autocorrelation function $C_{1,1}(t)$ for the disordered qubit ladder with $L = 12$ and $W_S/2\pi \leq 20$ MHz. **b** is similar to **a** but for the data with $W_S/2\pi \geq 24$ MHz. Markers (lines) are experimental (numerical) data. **c**, Transport exponent z as a function of W_S . For $W_S/2\pi \leq 20$ MHz and $W_S/2\pi \geq 24$ MHz, the exponent z is extracted from fitting the data of $C_{1,1}(t)$ with the time window $t \in [50\text{ns}, 200\text{ns}]$ and $t \in [100\text{ns}, 400\text{ns}]$, respectively. Error bars (experimental data) and shaded regions (numerical data) represent the standard deviation.

transport in other systems with ergodicity breaking.

Subdiffusive transport with ergodicity breaking

After demonstrating that the quantum circuit shown in Fig. 1c can be employed to measure the infinite-temperature autocorrelation function $C_{1,1}$, we study spin transport on the superconducting qubit ladder with disorder, whose effective Hamiltonian can be written as $\hat{H}_D = \hat{H}_I + \sum_{m \in \{\uparrow, \downarrow\}} \sum_{j=1}^L w_{j,m} \hat{\sigma}_{j,m}^+ \hat{\sigma}_{j,m}^-$, with $w_{j,m}$ drawn from a uniform distribution $[-W, W]$, and W being the strength of disorder. The results of $C_{1,1}$ with different W are plotted in Fig. 3a. With the increasing of W , and as the system approaches the MBL transition, $C_{1,1}$ decays more slowly. We then fit both the experimental and numerical data with the time window $t \in [50\text{ ns}, 200\text{ ns}]$ by adopting the power-law decay $C_{1,1} \propto t^{-z}$. As shown in Fig. 3b, we observe an anomalous subdiffusive region with the transport exponent $z < 1/2$. For the strength of disorder $W/2\pi \gtrsim 50$ MHz, the transport exponent $z \sim 10^{-2}$, indicating the freezing of spin transport and the onset of MBL on the 24-qubit system [2].

Next, we explore the transport properties on a titled superconducting qubit ladder, which is subjected to the linear potential $\hat{H}_L = \sum_{j=1}^L \gamma j \sum_{m \in \{\uparrow, \downarrow\}} \hat{\sigma}_{j,m}^+ \hat{\sigma}_{j,m}^-$, with $\gamma = 2W_S/(L-1)$ being the slope of the linear potential (see the titled ladder in the inset of Fig. 4a). Thus, the effective Hamiltonian of the titled superconducting qubit ladder can be written as $\hat{H}_T = \hat{H}_I + \hat{H}_L$. Different from the aforementioned breakdown of ergodicity induced by the disorder, the linear potential can also halt the onset of ergodic behaviors, resulting in the Stark MBL in disorder-free systems [24, 44–48].

We employ the method based on the quantum cir-

cuit shown in Fig. 1c to measure the time evolution of the autocorrelation function $C_{1,1}$ with different slopes of the linear potential. The results are presented in Fig. 4a and 4b. Similar to the system with disorder, the dynamics of $C_{1,1}$ still satisfies $C_{1,1} \propto t^{-z}$ with $z < 0.5$, i.e., subdiffusive transport. Figure 4c displays the transport exponent z with different strength of the linear potential, showing that z asymptotically drops as W_S increases. By employing the same standard for the onset of MBL induced by disorder, i.e., $z \sim 10^{-2}$, the results in Fig. 4c indicate that the Stark MBL on the titled 24-qubit ladder occurs when $W_S/2\pi \gtrsim 80$ MHz ($\gamma/2\pi \gtrsim 14.6$ MHz).

Discussion

Based on the novel protocol for simulating the infinite-temperature spin transport using the Haar-random state [36], we have experimentally probed diffusive transport on a 24-qubit ladder-type programmable superconducting processor. Moreover, when the qubit ladder is subject to sufficiently strong disorder or linear potential, we observe the signatures of subdiffusive transport, in accompany with the breakdown of ergodicity due to the conventional or Stark MBL.

Ensembles of Haar-random pure quantum states have several promising applications, including benchmarking quantum devices [38, 54] and demonstrating the quantum advantage [31–35]. Our work displays a practical application of the randomly distributed quantum state, i.e., probing the infinite-temperature spin transport. In contrast to employing digital random circuits, where the number of imperfect two-qubit gates is proportional to the qubit number [32–37], the scalable analog circuit

adopted in our experiments can also generate multi-qubit Haar-random states useful for simulating hydrodynamics. The protocol employed in our work can be naturally extended to explore the non-trivial transport properties on other analog quantum simulators, including the Rydberg atoms [55–57], quantum gas microscopes [58], and the waveguide or cavity QED setups [59–62].

Methods

Derivation of Eq. (4)

Here, we present the details of the derivation of Eq. (4), which is based on the typicality [12, 36, 63]. According to Eq. (2), $c_{\alpha;\beta} = \text{Tr}[\hat{\sigma}_\alpha^z(t)\hat{\sigma}_\beta^z]/D$, with $D = 2^L$. We define $\hat{N}_\beta = (\hat{\sigma}_\beta^z + 1)/2$, and then $c_{\alpha;\beta} = \frac{2}{D} \text{Tr}[\hat{\sigma}_\alpha^z(t)\hat{N}_\beta]$. By using $\hat{N}_\beta = (\hat{N}_\beta)^2$, we have $c_{\alpha;\beta} = \frac{2}{D} \text{Tr}[\hat{N}_\beta \hat{\sigma}_\alpha^z(t)\hat{N}_\beta]$.

According to the typicality [12, 36, 63], the trace of an operator \hat{O} can be approximated as the expectation value averaged by the pure Haar-random state $|r\rangle$, i.e.,

$$\frac{1}{D} \text{Tr}[\hat{O}] \simeq \langle r | \hat{O} | r \rangle. \quad (5)$$

Thus, $c_{\alpha;\beta} \simeq 2 \langle r | \hat{N}_\beta \hat{\sigma}_\alpha^z(t) \hat{N}_\beta | r \rangle = \langle \psi_\beta^R(t) | \hat{\sigma}_\alpha^z | \psi_\beta^R(t) \rangle$.

Superconducting transmon qubit

A transmon qubit is composed of a capacitance C and a nonlinear inductance L (Josephson junction or SQUID). Its Lagrangian \mathcal{L}_0 and Hamiltonian H_0 can be written as

$$\mathcal{L}_0 = \frac{Q^2}{2C} - \frac{\Phi^2}{2L} \quad (6)$$

$$H_0 = \frac{Q^2}{2C} + \frac{\Phi^2}{2L}, \quad (7)$$

where $Q = \partial \mathcal{L}_0 / \partial \dot{\Phi} = C \dot{\Phi}$ denotes the charge, and Φ is the magnetic flux of the circuit. Here, the nonlinear inductance of the Josephson junction with energy E_J can be written as $L = L_c / \cos(2\pi\Phi/\Phi_0)$, where $\Phi_0 = \hbar\pi/e$ is the superconducting flux quantum, $e \approx 1.602 \times 10^{-19} \text{C}$ is the electron charge, and $L_c = \Phi_0^2 / (4\pi^2 E_J)$ is the constant inductance. This nonlinear inductance can be easily derived from the definition $L = d\Phi/dI$ and the Josephson equation $I = I_c \sin(2\pi\Phi/\Phi_0)$ with $I_c = 2\pi E_J / \Phi_0$ being the Josephson critical current.

Considering the weak flux Φ , one can use the approximation $\cos(2\pi\Phi/\Phi_0) \simeq 1 - (2\pi\Phi/\Phi_0)^2/2$ and reduce the Hamiltonian Eq. (7) into $H_0 \simeq \frac{Q^2}{2C} + \frac{\Phi^2}{2L_c} - \frac{\pi^2 \Phi^4}{4L_c \Phi_0^2}$, which can be viewed as a harmonic oscillator with $o(\Phi^4)$ perturbation. Using canonical quantization, one can introduce

$$\begin{cases} \hat{Q} = iQ_{\text{zpf}}(\hat{a}^\dagger - \hat{a}) \\ \hat{\Phi} = \Phi_{\text{zpf}}(\hat{a}^\dagger + \hat{a}) \end{cases} \quad (8)$$

with $Q_{\text{zpf}} = \sqrt{\hbar(C/L_c)^{1/2}/2}$ and $\Phi_{\text{zpf}} = \sqrt{\hbar(L_c/C)^{1/2}/2}$ being the zero point fluctuation of the charge and flux operators, respectively. The quantized Hamiltonian thus is (the constant term is omitted):

$$\hat{H}_0 = \hbar\omega \hat{a}^\dagger \hat{a} - \frac{E_C}{2} \hat{a}^\dagger \hat{a}^\dagger \hat{a} \hat{a}, \quad (9)$$

where $\omega = (\sqrt{8E_C E_J} - E_C)/\hbar$ denotes the qubit frequency, and $E_C = e^2/(2C)$ is the charging energy that represents the magnitude of anharmonicity. For a single Josephson junction, E_J is not tunable, while for a SQUID with two junctions, it depends on the external flux Φ_{ext} applied to the junction region. In the experiments, we can adjust the qubit frequency ω via the external fast flux bias applied to the Z control line.

XY drive in superconducting circuits

When a time-dependent driving voltage $V_d(t)$ is added to XY line of the qubit, the total Lagrangian is given by

$$\mathcal{L}_{\text{driven}} = \frac{1}{2} C \dot{\Phi}^2 + \frac{1}{2} C_d (V_d(t) - \dot{\Phi})^2 - \frac{\Phi^2}{2L}, \quad (10)$$

where C_d is the driving capacitance. The Lagrangian $\mathcal{L}_{\text{driven}}$ can be verified by the Kirchhoff laws for this driven system.

To obtain the Hamiltonian, we first calculate the conjugate to the position (flux) Φ , namely the canonical momentum (charge) $\tilde{Q} = \partial \mathcal{L}_{\text{driven}} / \partial \dot{\Phi} = C_\Sigma \dot{\Phi} - C_d V_d(t)$, and thus

$$H_{\text{driven}} = \tilde{Q} \dot{\Phi} - \mathcal{L}_{\text{driven}} = \frac{\tilde{Q}^2}{2C_\Sigma} + \frac{\Phi^2}{2L} + \frac{\tilde{Q} C_d V_d(t)}{C_\Sigma}. \quad (11)$$

Using the canonical quantization procedure like Eq. (8), we introduce $\hat{\tilde{Q}} = i\tilde{Q}_{\text{zpf}}(\hat{a}^\dagger - \hat{a})$ and $\hat{\Phi} = \Phi_{\text{zpf}}(\hat{a}^\dagger + \hat{a})$ to quantize the driven system, where $\tilde{Q}_{\text{zpf}} = \sqrt{\hbar(C_\Sigma/L_c)^{1/2}/2}$ and $\Phi_{\text{zpf}} = \sqrt{\hbar(L_c/C_\Sigma)^{1/2}/2}$. Hence, the Hamiltonian becomes

$$\hat{H}_{\text{driven}} = \hbar\omega \hat{a}^\dagger \hat{a} - \frac{E_C}{2} \hat{a}^\dagger \hat{a}^\dagger \hat{a} \hat{a} + i\hbar\Omega(t)(\hat{a}^\dagger - \hat{a}), \quad (12)$$

where $E_C = e^2/(2C_\Sigma)$, $E_J = \Phi_0^2/4\pi^2 L_c$, $\omega = \sqrt{8E_C E_J} - E_C$, $\Omega(t) = \epsilon V_d(t)$, $\epsilon = \tilde{Q}_{\text{zpf}} C_d / (\hbar C_\Sigma)$. Here, we set the time-dependent driving $V_d(t) = -V_d \sin(\omega_d t + \phi) = \text{Im}\{V_d e^{-i(\omega_d t + \phi)}\}$, thus $\Omega(t) = i\Omega(e^{-i(\omega_d t + \phi)} - e^{i(\omega_d t + \phi)})/2$, where $\Omega = \epsilon V_d$ is so-called Rabi frequency. The parameter ϵ represents the Rabi frequency corresponding to the unit amplitude of the drive.

To solve the time evolution governed by the above time-dependent Hamiltonian, we consider the rotating

frame which is generated by $\hat{U}_d(t) = e^{i\omega_d t \hat{a}^\dagger \hat{a}}$

$$\begin{aligned}\hat{H}_d &= \hat{U}_d(t) \hat{H}_{\text{driven}}(t) \hat{U}_d^\dagger(t) + i\hbar \left(\frac{d}{dt} \hat{U}_d(t) \right) \hat{U}_d^\dagger(t) \\ &\simeq \hbar \Delta \hat{a}^\dagger \hat{a} - \frac{E_C}{2} \hat{a}^\dagger \hat{a}^\dagger \hat{a} \hat{a} + \frac{\hbar \Omega}{2} (\hat{a}^\dagger e^{-i\phi} + \hat{a} e^{i\phi})\end{aligned}\quad (13)$$

where $\Delta = \omega - \omega_d$ is the frequency detuning, and the rotating-wave approximation is adopted by ignoring high frequency oscillation $\pm 2\omega_d$.

With $\Delta = 0$ and $E_C \gg \Omega$, the large anharmonicity results in the resonant drive acting almost exclusively between the first two energy levels $|0\rangle$ and $|1\rangle$ without leakage to higher levels. Hence, considering the two-level qubit, we have

$$\hat{H}_d = \frac{\hbar \Omega}{2} (\hat{\sigma}^+ e^{-i\phi} + \hat{\sigma}^- e^{i\phi}), \quad (14)$$

where $\hat{\sigma}_j^+$ ($\hat{\sigma}_j^-$) is the raising (lowering) operator. If the qubit begins in the ground state $|0\rangle$, its time-dependent state during the unitary evolution is

$$|\psi_d(t)\rangle = e^{-\frac{i}{\hbar} \hat{H}_d t} |0\rangle = \cos \frac{\Omega t}{2} |0\rangle - i e^{i\phi} \sin \frac{\Omega t}{2} |1\rangle, \quad (15)$$

and the probability of qubit in $|1\rangle$ is given by $P_1(t) = \sin^2(\Omega t/2) = [1 - \cos(\Omega t)]/2$. Considering the energy relaxation, the envelope of $P_1(t)$ will decay in a dissipative evolution and thus

$$P_1(t) = \frac{1}{2} \left[1 - e^{-\frac{t}{T_1}} \cos(\Omega t) \right], \quad (16)$$

where T_1 is the energy relaxation time that depends on the qubit frequency ω . In order to obtain the Rabi frequency Ω , one can fit the data of $P_1(t)$ by using the form of function $A \exp(-t/T_1) \cos(\Omega t) + B$. Typical experimental data of calibrating XY drive with different driving amplitudes are displayed in Extended Data Fig. 1.

The above results are based on the resonance condition $\omega = \omega_d$. If the detuning $\Delta = \omega - \omega_d \neq 0$, the effective Rabi frequency will be $\Omega_R = \sqrt{\Delta^2 + \Omega^2}$. Therefore, to obtain the correct Rabi frequency when $\omega = \omega_d$, we should find the corresponding Z pulse amplitude that makes the qubit resonate with the microwave before calibrating XY drive. This step can be easily achieved via spectroscopy experiment or Rabi oscillation by scanning the Z pulse amplitude of the qubit.

Microwave crosstalk and correction

Consider two driven qubits Q_i and Q_j coupled by a coupling capacitance C_{ij} , the quantized Hamiltonian is

(see Supplementary Section IV)

$$\hat{H}_{\text{driven}}^{(i,j)} = \hat{H}_{\text{driven}}^{(i)} + \hat{H}_{\text{driven}}^{(j)} + \hat{H}_{\text{int}}^{(i,j)}, \quad (17)$$

$$\begin{aligned}\hat{H}_{\text{driven}}^{(q)} &= \hbar \omega_q \hat{a}_q^\dagger \hat{a}_q - \frac{E_{C_q}}{2} \hat{a}_q^\dagger \hat{a}_q^\dagger \hat{a}_q \hat{a}_q \\ &\quad + i\hbar \tilde{\Omega}_q(t) (\hat{a}_q^\dagger - \hat{a}_q), \quad q \in \{i, j\},\end{aligned}\quad (18)$$

$$\hat{H}_{\text{int}}^{(i,j)} = \hbar J_{i,j} (\hat{a}_i^\dagger - \hat{a}_i) (\hat{a}_j - \hat{a}_j^\dagger), \quad (19)$$

where $J_{i,j}$ is the coupling strength and

$$\tilde{\Omega}_i(t) = \epsilon_{ii} \left(V_{d,i}(t) + \frac{\epsilon_{ij}}{\epsilon_{ii}} V_{d,j}(t) \right), \quad (20)$$

$$\tilde{\Omega}_j(t) = \epsilon_{jj} \left(V_{d,j}(t) + \frac{\epsilon_{ji}}{\epsilon_{jj}} V_{d,i}(t) \right). \quad (21)$$

The parameters ϵ_{ij} and ϵ_{ji} are explained in Supplementary Section IV, which depends on the coupling capacitance C_{ij} between the two qubits. Here, we focus on the origin of the crosstalk. Given the above equations, we note that the local driving Hamiltonian of each qubit is subject to both external drive $V_{d,i}(t)$ and $V_{d,j}(t)$ due to the presence of coupling capacitance. However, this crosstalk is usually very small. In fact, most of the crosstalk comes from the classical microwave crosstalk. The total crosstalk is the sum of the classical microwave crosstalk and the crosstalk due to the coupling capacitance. In the following, we will establish a model to describe the total crosstalk and introduce an efficient method for measuring the crosstalk matrix.

When the microwave signal travels through the medium on the chip, it can be described by the plane wave form $V_d(\mathbf{r}, t) = V_d(t) e^{i\mathbf{k} \cdot \mathbf{r}}$. Here, the wave vector \mathbf{k} is generally complex, namely $\mathbf{k} = \mathbf{b} + i\mathbf{a}$, thus we have $i\mathbf{k} \cdot \mathbf{r} = -\mathbf{a} \cdot \mathbf{r} + i\mathbf{b} \cdot \mathbf{r}$, where the first term is the amplitude attenuation induced by the imaginary part of \mathbf{k} and the second term is the phase retardation caused by the real part.

As shown in Extended Data Fig. 2, the signal $V_{d,i}(t)$ propagates from Q_i to Q_j with a factor $e^{-\xi_{ji} + i\phi_{ji}}$ attached, which implies the classical microwave crosstalk of Q_i to Q_j . Similarly, the classical microwave crosstalk of Q_j to Q_i can be express as $V_{d,j}(t) e^{-\xi_{ij} + i\phi_{ij}}$. Moreover, the crosstalk caused by the coupling capacitance is also considered. Therefore, the total signals perceived by Q_i and Q_j are

$$\begin{bmatrix} \tilde{V}_{d,i}(t) \\ \tilde{V}_{d,j}(t) \end{bmatrix} = \begin{bmatrix} 1 & v_{ij} e^{i\phi_{ij}} \\ v_{ji} e^{i\phi_{ji}} & 1 \end{bmatrix} \begin{bmatrix} V_{d,i}(t) \\ V_{d,j}(t) \end{bmatrix} \quad (22)$$

with the definitions of $v_{ij} e^{i\phi_{ij}} = \epsilon_{ij}/\epsilon_{ii} + e^{-\xi_{ij} + i\phi_{ij}}$ and $v_{ji} e^{i\phi_{ji}} = \epsilon_{ji}/\epsilon_{jj} + e^{-\xi_{ji} + i\phi_{ji}}$. To generalize the above formula to the case of each qubit with crosstalks from all other qubits, we define the vectors

$\tilde{\mathbf{V}}_d(t) = [\tilde{V}_{d,1}(t), \tilde{V}_{d,2}(t), \dots, \tilde{V}_{d,N}(t)]^T$ and $\mathbf{V}_d(t) = [V_{d,1}(t), V_{d,2}(t), \dots, V_{d,N}(t)]^T$, then

$$\tilde{\mathbf{V}}_d(t) = \mathbf{M}_V \mathbf{V}_d(t), \quad (23)$$

in which \mathbf{M}_V is the signal crosstalk matrix

$$\mathbf{M}_V = \begin{bmatrix} 1 & v_{12}e^{i\varphi_{12}} & \dots & v_{1N}e^{i\varphi_{1N}} \\ v_{21}e^{i\varphi_{21}} & 1 & \dots & v_{2N}e^{i\varphi_{2N}} \\ \vdots & \vdots & \ddots & \vdots \\ v_{N1}e^{i\varphi_{N1}} & v_{N2}e^{i\varphi_{N2}} & \dots & 1 \end{bmatrix}. \quad (24)$$

To correct the crosstalk, one can measure the total signal crosstalk matrix and perform

$$\mathbf{V}_d(t) = \mathbf{M}_V^{-1} \tilde{\mathbf{V}}_d(t), \quad (25)$$

where \mathbf{M}_V^{-1} is the inverse matrix. However, in practice, the matrix \mathbf{M}_V cannot be directly measured. Thus, we need to measure the crosstalk matrix of Rabi frequencies \mathbf{M}_Ω and calculate \mathbf{M}_V by using

$$\mathbf{M}_V = \epsilon \mathbf{M}_\Omega \epsilon^{-1}, \quad (26)$$

where $\epsilon = \text{diag}\{\epsilon_{11}, \epsilon_{22}, \dots, \epsilon_{NN}\}$, and the crosstalk matrix of Rabi frequencies is defined as

$$\mathbf{M}_\Omega = \begin{bmatrix} 1 & c_{12}e^{i\varphi_{12}} & \dots & c_{1N}e^{i\varphi_{1N}} \\ c_{21}e^{i\varphi_{21}} & 1 & \dots & c_{2N}e^{i\varphi_{2N}} \\ \vdots & \vdots & \ddots & \vdots \\ c_{N1}e^{i\varphi_{N1}} & c_{N2}e^{i\varphi_{N2}} & \dots & 1 \end{bmatrix}. \quad (27)$$

Here, c_{ij} and φ_{ij} are the amplitude and phase crosstalk coefficients to be measured.

Measurement of crosstalk matrix

Now, we introduce an efficient method for measuring the crosstalk matrix. Let us take an example of Q_i . As shown in Extended Data Fig. 3a, two resonant microwave signals $\omega_{d,i} = \omega_{d,j} = \omega_d$ are simultaneously input from the XY control lines of Q_i and Q_j . Meanwhile, Q_i is biased near the resonant frequency with the detuning $\Delta_i = \omega_i - \omega_{d,i}$. Due to the crosstalk, the

effective Hamiltonian of Q_i under the rotation frame becomes $\hat{H}_d^{(i)} = \Delta_i \hat{\sigma}_i^+ \hat{\sigma}_i^- + (\tilde{\Omega}_i \hat{\sigma}_i^+ + \text{H.c.})/2$ with $\tilde{\Omega}_i = \Omega_i e^{-i\phi_i} + c_{ij} \Omega_j e^{i(\varphi_{ij} - \phi_j)}$, and the corresponding effective Rabi frequency is

$$\Omega_R^{(i)} = \sqrt{\Delta_i^2 + \Omega_i^2 + \Omega_{ij}^2 + 2\Omega_i \Omega_{ij} \cos(\varphi_{ij} - \varphi_{ii})}, \quad (28)$$

where $\Omega_{ij} = c_{ij} \Omega_j$ denotes the crosstalk Rabi frequency from Q_j to Q_i , and $\varphi_{ii} = \phi_j - \phi_i$ represents the additional XY phase added in Q_i relative to Q_j . By scanning φ_{ii} and measure the probabilities of Q_i in $|1\rangle$ as a function of the duration of XY drive, we can obtain $\Omega_R^{(i)}$. Using Eq. (28) to fit the results of $\Omega_R^{(i)}$, we can determine the crosstalk coefficients c_{ij} and φ_{ij} . The procedure for determining c_{ji} and φ_{ji} is similar as long as we treat Q_j as Q_i .

Numerical simulations

Here, we present the details of the numerical simulations. We calculate the unitary time evolution $|\psi(t + \Delta t)\rangle = e^{-i\hat{H}\Delta t}|\psi(t)\rangle$ by employing the Krylov method [43]. The Krylov subspace is panned by the vectors defined as $\{|\psi(t)\rangle, \hat{H}|\psi(t)\rangle, \hat{H}^2|\psi(t)\rangle, \dots, \hat{H}^{(m-1)}|\psi(t)\rangle\}$. Then, the Hamiltonian \hat{H} in the Krylov subspace becomes a m -dimensional matrix $H_m = \mathbf{K}_m^\dagger \mathbf{H} \mathbf{K}_m$, where \mathbf{H} denotes the Hamiltonian \hat{H} in the matrix form, and \mathbf{K}_m is the matrix whose columns contain the orthonormal basis vectors of the Krylov space. Finally, the unitary time evolution can be approximately simulated in the Krylov subspace as $|\psi(t + \Delta t)\rangle \simeq \mathbf{K}_m^\dagger e^{-iH_m \Delta t} \mathbf{K}_m |\psi(t)\rangle$. In our numerical simulations, the dimension of the Krylov subspace m is adaptively adjusted from $m = 6$ to 30, making sure the numerical errors are smaller than 10^{-14} .

For the numerical simulation of the $\hat{U}_R(t_R) = e^{-i\hat{H}_d t_R}$ in Fig. 1c, based on the experimental data of the XY drive, the parameters in \hat{H}_d are $\Omega_{j,m}/2\pi = 10.4 \pm 1.6$ MHz, and $\phi_{j,m} \in [-\pi/10, \pi/10]$.

-
- [1] R. Nandkishore and D. A. Huse, “Many-body localization and thermalization in quantum statistical mechanics,” *Annual Review of Condensed Matter Physics* **6**, 15–38 (2015).
 - [2] K. Agarwal, S. Gopalakrishnan, M. Knap, M. Müller, and E. Demler, “Anomalous diffusion and griffiths effects near the many-body localization transition,” *Phys. Rev. Lett.* **114**, 160401 (2015).
 - [3] M. Žnidarič, A. Scardicchio, and V. K. Varma, “Diffusive and subdiffusive spin transport in the ergodic phase of a many-body localizable system,” *Phys. Rev. Lett.* **117**, 040601 (2016).
 - [4] M. Ljubotina, J.-Y. Desautels, M. Serbyn, and Z. Papić, “Superdiffusive energy transport in kinetically constrained models,” *Phys. Rev. X* **13**, 011033 (2023).
 - [5] A. Scheie, N. E. Sherman, M. Dupont, S. E. Nagler, M. B. Stone, G. E. Granroth, J. E. Moore, and D. A. Tennant, “Detection of kardar-parisi-zhang hydrodynamics

- in a quantum heisenberg spin-1/2 chain,” *Nature Physics* **17**, 726–730 (2021).
- [6] M. Žnidarič, “Spin transport in a one-dimensional anisotropic heisenberg model,” *Phys. Rev. Lett.* **106**, 220601 (2011).
- [7] M. Dupont, N. E. Sherman, and J. E. Moore, “Spatiotemporal crossover between low- and high-temperature dynamical regimes in the quantum heisenberg magnet,” *Phys. Rev. Lett.* **127**, 107201 (2021).
- [8] B. Bertini, F. Heidrich-Meisner, C. Karrasch, T. Prosen, R. Steinigeweg, and M. Žnidarič, “Finite-temperature transport in one-dimensional quantum lattice models,” *Rev. Mod. Phys.* **93**, 025003 (2021).
- [9] J. Eisert, M. Friesdorf, and C. Gogolin, “Quantum many-body systems out of equilibrium,” *Nature Physics* **11**, 124–130 (2015).
- [10] P. Peng, B. Ye, N. Y. Yao, and P. Cappellaro, “Exploiting disorder to probe spin and energy hydrodynamics,” *Nature Physics* (2023).
- [11] R. Steinigeweg, F. Heidrich-Meisner, J. Gemmer, K. Michielsen, and H. De Raedt, “Scaling of diffusion constants in the spin- $\frac{1}{2}$ xx ladder,” *Phys. Rev. B* **90**, 094417 (2014).
- [12] D. Schubert, J. Richter, F. Jin, K. Michielsen, H. De Raedt, and R. Steinigeweg, “Quantum versus classical dynamics in spin models: Chains, ladders, and square lattices,” *Phys. Rev. B* **104**, 054415 (2021).
- [13] M. Ljubotina, M. Žnidarič, and T. Prosen, “Spin diffusion from an inhomogeneous quench in an integrable system,” *Nature Communications* **8**, 16117 (2017).
- [14] D. Wei *et al.*, “Quantum gas microscopy of kardar-parisi-zhang superdiffusion,” *Science* **376**, 716–720 (2022).
- [15] M. K. Joshi *et al.*, “Observing emergent hydrodynamics in a long-range quantum magnet,” *Science* **376**, 720–724 (2022).
- [16] Elliott Rosenberg *et al.*, “Dynamics of magnetization at infinite temperature in a Heisenberg spin chain,” *arXiv e-prints*, arXiv:2306.09333 (2023).
- [17] J. Feldmeier, P. Sala, G. De Tomasi, F. Pollmann, and M. Knap, “Anomalous diffusion in dipole- and higher-moment-conserving systems,” *Phys. Rev. Lett.* **125**, 245303 (2020).
- [18] J. De Nardis, S. Gopalakrishnan, R. Vasseur, and B. Ware, “Subdiffusive hydrodynamics of nearly integrable anisotropic spin chains,” *Proceedings of the National Academy of Sciences* **119**, e2202823119 (2022).
- [19] A. Gromov, A. Lucas, and R. M. Nandkishore, “Fracton hydrodynamics,” *Phys. Rev. Res.* **2**, 033124 (2020).
- [20] F. Chen *et al.*, “Observation of strong and weak thermalization in a superconducting quantum processor,” *Phys. Rev. Lett.* **127**, 020602 (2021).
- [21] Q. Zhu *et al.*, “Observation of thermalization and information scrambling in a superconducting quantum processor,” *Phys. Rev. Lett.* **128**, 160502 (2022).
- [22] P. Roushan *et al.*, “Spectroscopic signatures of localization with interacting photons in superconducting qubits,” *Science* **358**, 1175–1179 (2017).
- [23] Q. Guo *et al.*, “Observation of energy-resolved many-body localization,” *Nature Physics* **17**, 234–239 (2021).
- [24] Q. Guo *et al.*, “Stark many-body localization on a superconducting quantum processor,” *Phys. Rev. Lett.* **127**, 240502 (2021).
- [25] P. Zhang *et al.*, “Many-body hilbert space scarring on a superconducting processor,” *Nature Physics* **19**, 120–125 (2023).
- [26] X. Zhang *et al.*, “Digital quantum simulation of floquet symmetry-protected topological phases,” *Nature* **607**, 468–473 (2022).
- [27] X. Mi *et al.*, “Time-crystalline eigenstate order on a quantum processor,” *Nature* **601**, 531–536 (2022).
- [28] P. Frey and S. Rachel, “Realization of a discrete time crystal on 57 qubits of a quantum computer,” *Science Advances* **8**, eabm7652 (2022).
- [29] X. Mi *et al.*, “Information scrambling in quantum circuits,” *Science* **374**, 1479–1483 (2021).
- [30] J. Braumüller *et al.*, “Probing quantum information propagation with out-of-time-ordered correlators,” *Nature Physics* **18**, 172–178 (2022).
- [31] C. Neill *et al.*, “A blueprint for demonstrating quantum supremacy with superconducting qubits,” *Science* **360**, 195–199 (2018).
- [32] S. Boixo *et al.*, “Characterizing quantum supremacy in near-term devices,” *Nature Physics* **14**, 595–600 (2018).
- [33] F. Arute *et al.*, “Quantum supremacy using a programmable superconducting processor,” *Nature* **574**, 505–510 (2019).
- [34] Y. Wu *et al.*, “Strong quantum computational advantage using a superconducting quantum processor,” *Phys. Rev. Lett.* **127**, 180501 (2021).
- [35] A. Morvan *et al.*, “Phase transition in Random Circuit Sampling,” , arXiv:2304.11119 (2023).
- [36] J. Richter and A. Pal, “Simulating hydrodynamics on noisy intermediate-scale quantum devices with random circuits,” *Phys. Rev. Lett.* **126**, 230501 (2021).
- [37] N. Keenan, N. F. Robertson, T. Murphy, S. Zhuk, and J. Goold, “Evidence of kardar-parisi-zhang scaling on a digital quantum simulator,” *npj Quantum Information* **9**, 72 (2023).
- [38] Joonhee C. *et al.*, “Preparing random states and benchmarking with many-body quantum chaos,” *Nature* **613**, 468–473 (2023).
- [39] Z.-H. Sun, J. Cui, and H. Fan, “Characterizing the many-body localization transition by the dynamics of diagonal entropy,” *Phys. Rev. Res.* **2**, 013163 (2020).
- [40] I. Khait, S. Gazit, N. Y. Yao, and A. Auerbach, “Spin transport of weakly disordered heisenberg chain at infinite temperature,” *Phys. Rev. B* **93**, 224205 (2016).
- [41] S. Gopalakrishnan, K. Agarwal, E. A. Demler, D. A. Huse, and M. Knap, “Griffiths effects and slow dynamics in nearly many-body localized systems,” *Phys. Rev. B* **93**, 134206 (2016).
- [42] F. Setiawan, D.-L. Deng, and J. H. Pixley, “Transport properties across the many-body localization transition in quasiperiodic and random systems,” *Phys. Rev. B* **96**, 104205 (2017).
- [43] D. J. Luitz and Y. B. Lev, “The ergodic side of the many-body localization transition,” *Annalen der Physik* **529**, 1600350 (2017).

- [44] W. Morong *et al.*, “Observation of stark many-body localization without disorder,” *Nature* **599**, 393–398 (2021).
- [45] M. Schulz, C. A. Hooley, R. Moessner, and F. Pollmann, “Stark many-body localization,” *Phys. Rev. Lett.* **122**, 040606 (2019).
- [46] E. van Nieuwenburg, Y. Baum, and G. Refael, “From bloch oscillations to many-body localization in clean interacting systems,” *Proceedings of the National Academy of Sciences* **116**, 9269–9274 (2019).
- [47] Y.-Y. Wang, Z.-H. Sun, and H. Fan, “Stark many-body localization transitions in superconducting circuits,” *Phys. Rev. B* **104**, 205122 (2021).
- [48] S. R. Taylor, M. Schulz, F. Pollmann, and R. Moessner, “Experimental probes of stark many-body localization,” *Phys. Rev. B* **102**, 054206 (2020).
- [49] E. V. H. Doggen, I. V. Gornyi, and D. G. Polyakov, “Stark many-body localization: Evidence for hilbert-space shattering,” *Phys. Rev. B* **103**, L100202 (2021).
- [50] V. Khemani, M. Hermele, and R. Nandkishore, “Localization from hilbert space shattering: From theory to physical realizations,” *Phys. Rev. B* **101**, 174204 (2020).
- [51] P. Sala, T. Rakovszky, R. Verresen, M. Knap, and F. Pollmann, “Ergodicity breaking arising from hilbert space fragmentation in dipole-conserving hamiltonians,” *Phys. Rev. X* **10**, 011047 (2020).
- [52] Z.-C. Xiang *et al.*, “Simulating chern insulators on a superconducting quantum processor,” *Nature Communications* **14**, 5433 (2023).
- [53] X. Gu, A. F. Kockum, A. Miranowicz, Y.-x. Liu, and F. Nori, “Microwave photonics with superconducting quantum circuits,” *Physics Reports* **718-719**, 1–102 (2017).
- [54] A. W. Cross, L. S. Bishop, S. Sheldon, P. D. Nation, and J. M. Gambetta, “Validating quantum computers using randomized model circuits,” *Phys. Rev. A* **100**, 032328 (2019).
- [55] M. Saffman, T. G. Walker, and K. Mølmer, “Quantum information with rydberg atoms,” *Rev. Mod. Phys.* **82**, 2313–2363 (2010).
- [56] A. Browaeys and T. Lahaye, “Many-body physics with individually controlled rydberg atoms,” *Nature Physics* **16**, 132–142 (2020).
- [57] L. Henriet, L. Beguin, A. Signoles, T. Lahaye, A. Browaeys, G.-O. Reymond, and C. Jurczak, “Quantum computing with neutral atoms,” *Quantum* **4**, 327 (2020).
- [58] C. Gross and I. Bloch, “Quantum simulations with ultracold atoms in optical lattices,” *Science* **357**, 995–1001 (2017).
- [59] D. Ballester, G. Romero, J. J. García-Ripoll, F. Deppe, and E. Solano, “Quantum simulation of the ultrastrong-coupling dynamics in circuit quantum electrodynamics,” *Phys. Rev. X* **2**, 021007 (2012).
- [60] K. Xu *et al.*, “Probing dynamical phase transitions with a superconducting quantum simulator,” *Sci. Adv.* **6**, eaba4935 (2020).
- [61] K. Xu *et al.*, “Metrological characterization of non-gaussian entangled states of superconducting qubits,” *Phys. Rev. Lett.* **128**, 150501 (2022).
- [62] X. Zhang, E. Kim, D. K. Mark, S. Choi, and O. Painter, “A superconducting quantum simulator based on a photonic-bandgap metamaterial,” *Science* **379**, 278–283 (2023).
- [63] F. Jin, D. Willsch, M. Willsch, H. Lagemann, K. Michielsen, and H. De Raedt, “Random state technology,” *Journal of the Physical Society of Japan* **90**, 012001 (2020).

Data availability

All data needed to evaluate the conclusions in the paper are present in the paper and/or the Supplementary Information.

Acknowledgments

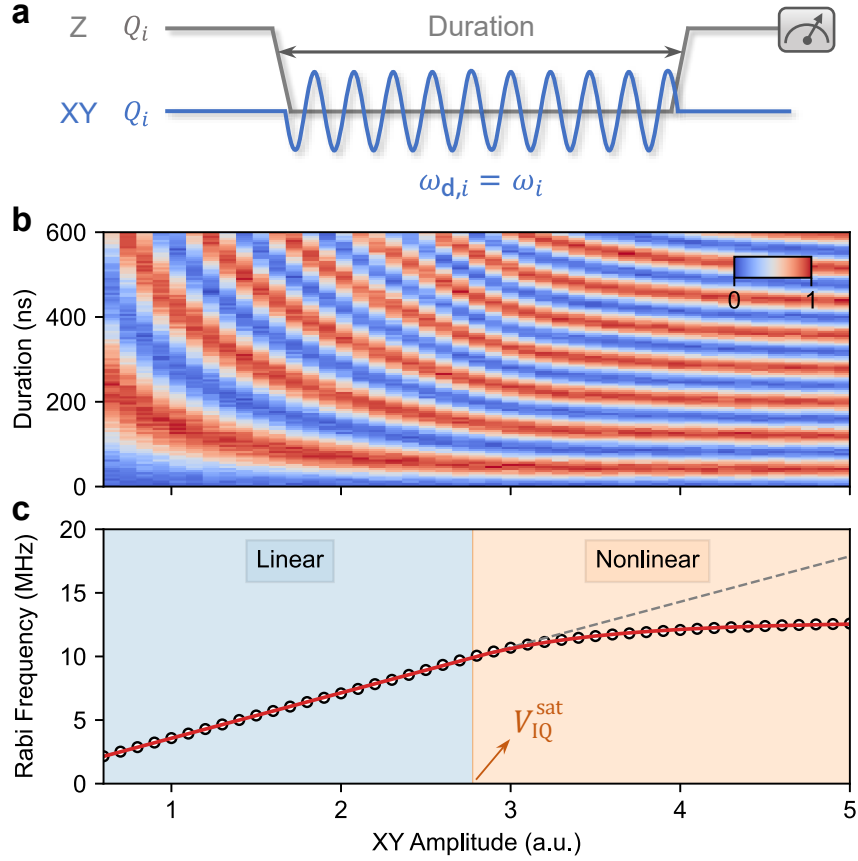
We thank Hai-Long Shi and H. S. Yan for helpful discussions. This work was supported by National Natural Science Foundation of China (Grants Nos. 11934018, 92265207, T2121001, 12122504, 12247168), Beijing Natural Science Foundation (Grant No. Z2000009), Innovation Program for Quantum Science and Technology (Grant No. 2021ZD0301800), Beijing Nova Program (No. 20220484121), Scientific Instrument Developing Project of Chinese Academy of Sciences (Grant No. YJKYYQ20200041), and China Postdoctoral Science Foundation (Certificate Number: 2022TQ0036).

Author contributions

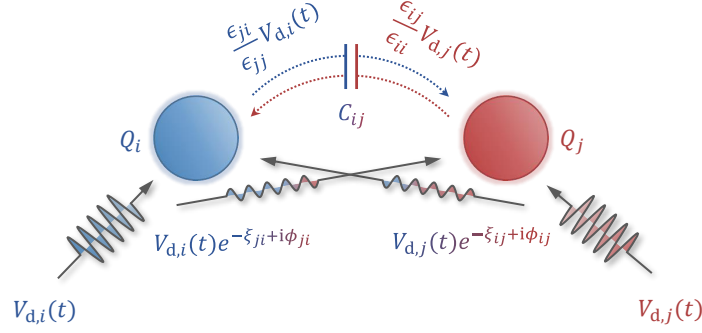
H.F. supervised the project. Z.-H.S. proposed the idea. Y.-H.S. conducted the experiment with the help of K.H. and K.X.. Z.-H.S., Y.-Y.W., and Y.-H.S. performed the numerical simulations. Z.X. and D.Z. fabricated the ladder-type sample. X.S., G.X., and H.Y. provided the Josephson parametric amplifiers. W.-G.M., H.-T.L., K.Z., J.-C.S., G.-H.L., Z.-Y.M., J.-C.Z., H.L., and C.-T.C. helped the experimental setup. Z.-A.W., Y.-R.Z., J.W., K.X., and H.F. discussed and commented on the manuscript. Z.-H.S., Y.-H.S., Y.-Y.W., Y.-R.Z., and H.F. co-wrote the manuscript. All authors contributed to the discussions of the results and development of the manuscript.

Competing interests

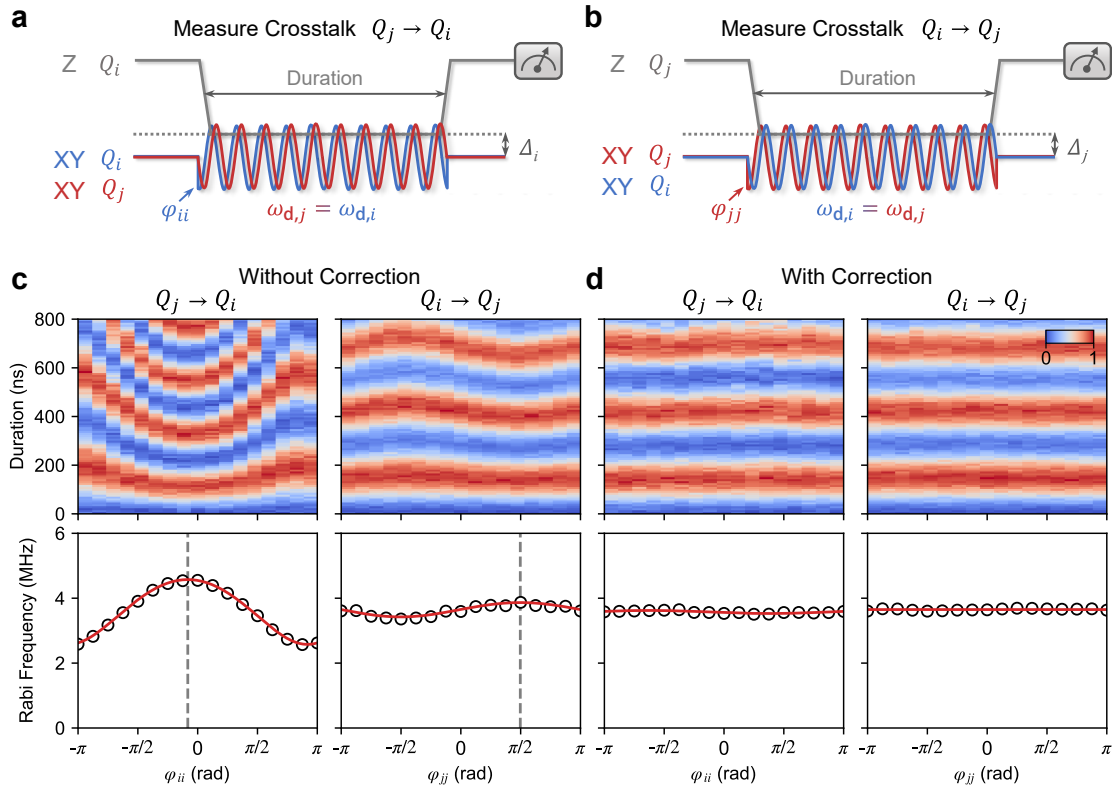
The authors declare no competing interests.



Extended data Fig. 1. Typical experimental data of measuring the relationship between Rabi frequency and XY drive amplitude. **a**, Experimental pulse sequence. Qubit is detuned from its idle frequency to the operating ω_i . Meanwhile, we apply resonant microwave drives on this qubit with scanning XY amplitude V_{IQ} and measure the vacuum Rabi oscillations shown in **b**. **b**, The heatmap of the probabilities of qubit in the state $|1\rangle$ as a function of duration and XY amplitude. **c**, For each XY drive amplitude, we fit the curve of vacuum Rabi oscillation by using Eq. (16) to obtain the experimental Rabi frequency, denoted as black hollow circle. The red solid line is the result of fitting the experimental Rabi frequencies by using a smooth piecewise function and the grey dashed line implies the linear relationship between Rabi frequency and XY drive amplitude when the drive amplitude is less than V_{IQ}^{sat} .



Extended data Fig. 2. Schematic of microwave signal crosstalk. Here, we take two qubits Q_i and Q_j as an example. Their individual driving voltages $V_{d,i}(t)$ and $V_{d,j}(t)$ induce two types of crosstalk. One type of crosstalk is due to the presence of coupling capacitance C_{ij} , which causes the crosstalk only in amplitude. The parameters ϵ_{ij} and ϵ_{ji} are explained in Supplementary Section IV, which depends on the coupling capacitance C_{ij} between the two qubits. The other type of crosstalk is caused by the propagation of microwave signals through the medium on the chip. According to electrodynamics, it will lead to the crosstalk both in amplitude and phase. The parameters ξ and ϕ are the amplitude attenuation factor and phase retardation of microwave propagation, respectively.



Extended data Fig. 3. Measurement of the microwave crosstalk. **a**, Experimental pulse sequence for measuring the crosstalk from Q_j to Q_i . **b**, Experimental pulse sequence for measuring the crosstalk from Q_i to Q_j . The parameters φ_{ii} and φ_{jj} denote the additional phases added into the XY control lines of Q_i and Q_j , respectively. The detuning between the qubit frequency and XY drive frequency is defined as $\Delta_q = \omega_q - \omega_{d,q}$, which is usually set to zero. **c**, Typical experimental data of measuring crosstalk without correction. **d**, Typical experimental data of measuring crosstalk with correction. The heatmap represents the probabilities of qubit in $|1\rangle$. The black hollow circle denotes the effective Rabi frequency obtained by fitting the Rabi oscillation. The red solid line is the result of fitting the effective Rabi frequency by using Eq. (28). The grey dashed line implies the fitted crosstalk phase.

Supplementary Information for Probing spin hydrodynamics on a superconducting quantum simulator

Yun-Hao Shi,^{1,2,3,*} Zheng-Hang Sun,^{1,2,*} Yong-Yi Wang,^{1,2,*} Zheng-An Wang,^{3,4} Yu-Ran Zhang,⁵ Wei-Guo Ma,^{1,2} Hao-Tian Liu,^{1,2} Kui Zhao,³ Jia-Cheng Song,^{1,2} Gui-Han Liang,^{1,2} Zheng-Yang Mei,^{1,2} Jia-Chi Zhang,^{1,2} Hao Li,¹ Chi-Tong Chen,^{1,2} Xiaohui Song,¹ Jieci Wang,⁶ Guangming Xue,³ Haifeng Yu,³ Kaixuan Huang,^{3,†} Zhongcheng Xiang,^{1,2,‡} Kai Xu,^{1,2,3,4,7,8,§} Dongning Zheng,^{1,2,4,7,8} and Heng Fan^{1,2,3,4,7,8,¶}

¹*Institute of Physics, Chinese Academy of Sciences, Beijing 100190, China*

²*School of Physical Sciences, University of Chinese Academy of Sciences, Beijing 100049, China*

³*Beijing Academy of Quantum Information Sciences, Beijing 100193, China*

⁴*Hefei National Laboratory, Hefei 230088, China*

⁵*School of Physics and Optoelectronics, South China University of Technology, Guangzhou 510640, China*

⁶*Department of Physics and Key Laboratory of Low Dimensional Quantum Structures and Quantum Control of Ministry of Education, Hunan Normal University, Changsha, Hunan 410081, China*

⁷*Songshan Lake Materials Laboratory, Dongguan, Guangdong 523808, China*

⁸*CAS Center for Excellence in Topological Quantum Computation, UCAS, Beijing 100190, China*

CONTENTS

I. Model and Hamiltonian	9
II. Wiring information	9
III. Lagrangian and Hamiltonian of single driven qubit	10
IV. Two coupled driven qubits	10
V. Generation of XY drive pulse	11
VI. XY drive approach to pseudo-random states	12
VII. Additional numerics and discussions	12

* These authors contributed equally to this work.

† huangkx@baqis.ac.cn

‡ zcxiang@iphy.ac.cn

§ kaixu@iphy.ac.cn

¶ hfan@iphy.ac.cn

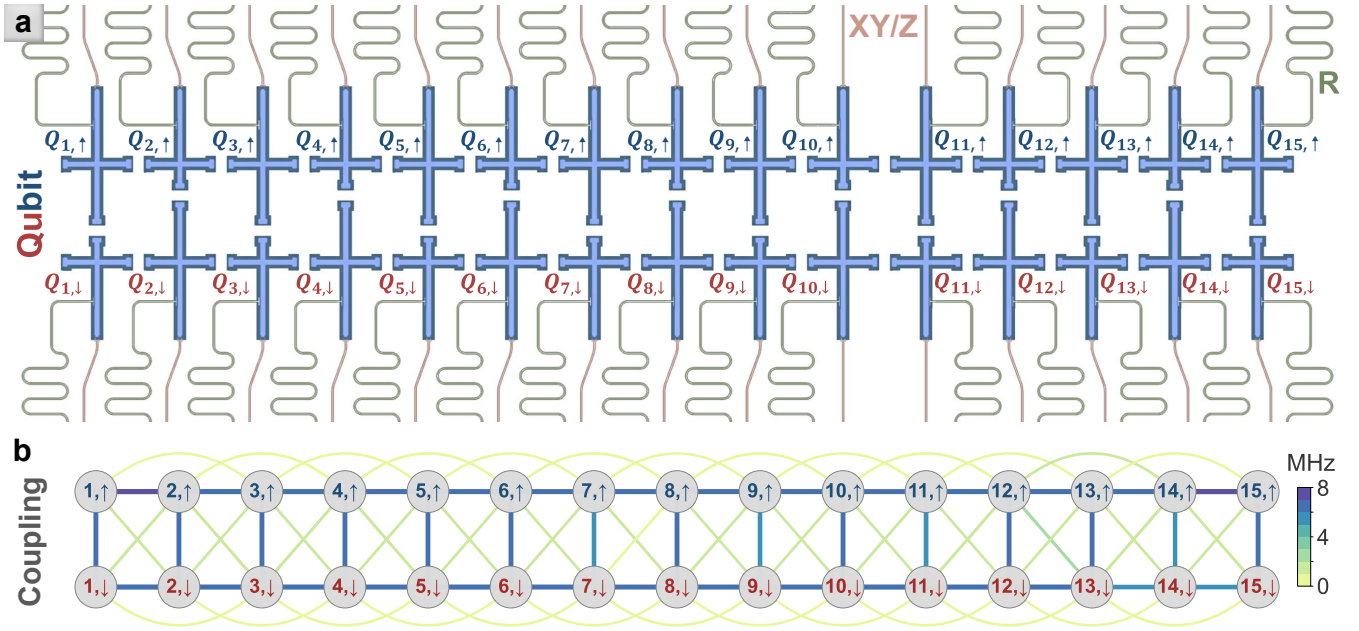


FIG. S1. **The optical micrograph and coupling strengths of the chip.** **a**, The ladder-type chip with 30 superconducting qubits arranged in two coupled chains. Each qubit, coupled to an independent readout resonator R, has an independent microwave line for XY and Z controls. **b**, Coupling strengths including the NN and NNN hopping couplings, which are measured by swapping experiments at the resonant frequency $\omega_{\text{ref}} \approx 4.534\text{GHz}$.

Parameter	Median	Mean	Stdev.	Units
Qubit maximum frequency	5.025	5.032	0.240	GHz
Qubit idle frequency	4.723	4.728	0.346	GHz
Qubit anharmonicity $-E_C/(2\pi)$	-0.222	-0.222	0.022	GHz
Readout frequency	6.715	6.714	0.061	GHz
Mean energy relaxation time \bar{T}_1	33.2	32.1	7.5	μs
Pure dephasing time at idle frequency T_2^*	1.0	2.4	4.2	μs

TABLE S1. List of device parameters.

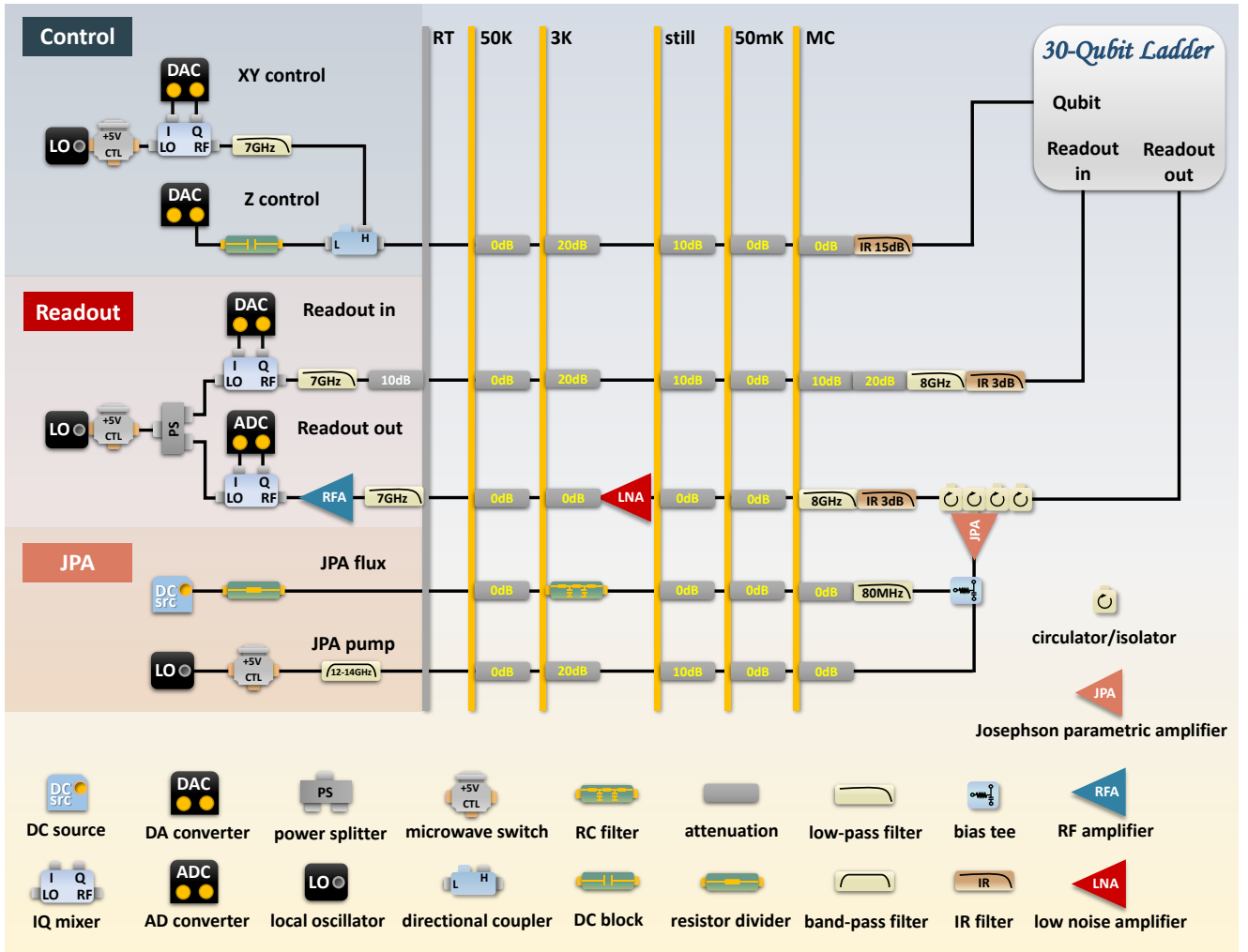


FIG. S2. Schematic diagram of the experimental system and wiring information.

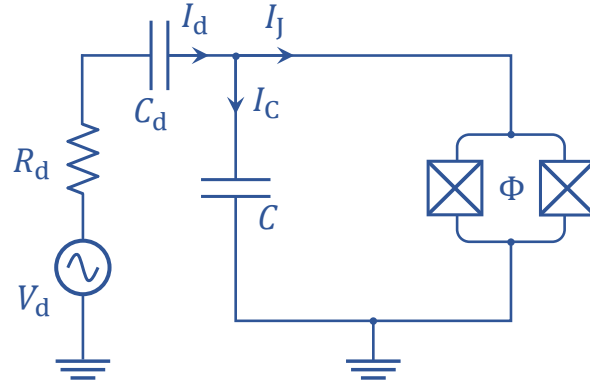


FIG. S3. **Circuit diagram of a superconducting transmon qubit.** The qubit is coupled to a time-dependent driving voltage V_d . The capacitances of the qubit and the drive are labeled as C and C_d , respectively. The magnetic flux threading the loop is denoted as Φ . The driving current I_d is split into I_C and I_J .

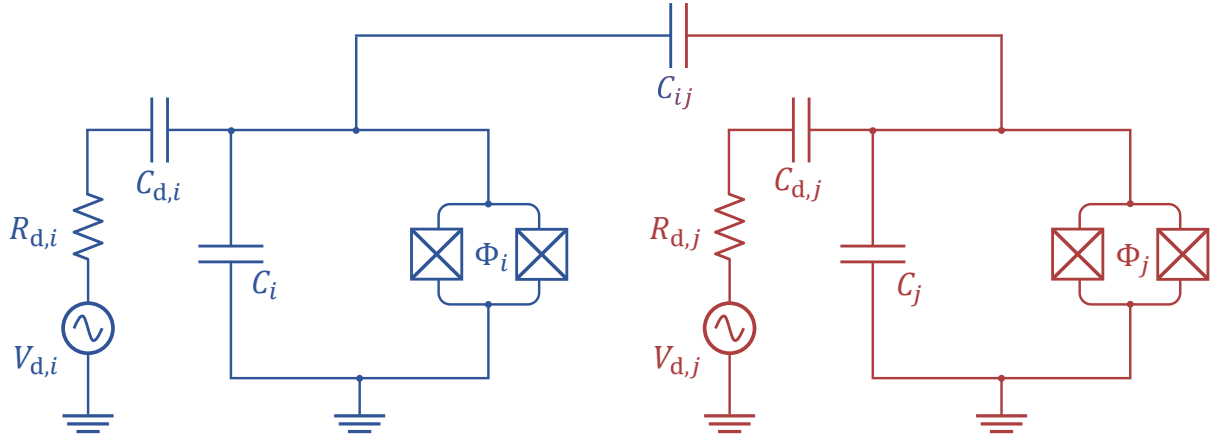


FIG. S4. **Circuit diagram of two superconducting transmon qubits.** Two qubits are labeled as Q_i and Q_j , which are coupled to their respective time-dependent driving voltages $V_{d,i}(t)$ and $V_{d,j}(t)$. The coupling capacitance between the two qubits is represented as C_{ij} , and Φ , C and C_d are the dominant mode flux, the capacitance of the qubit and the capacitance of the drive, respectively.

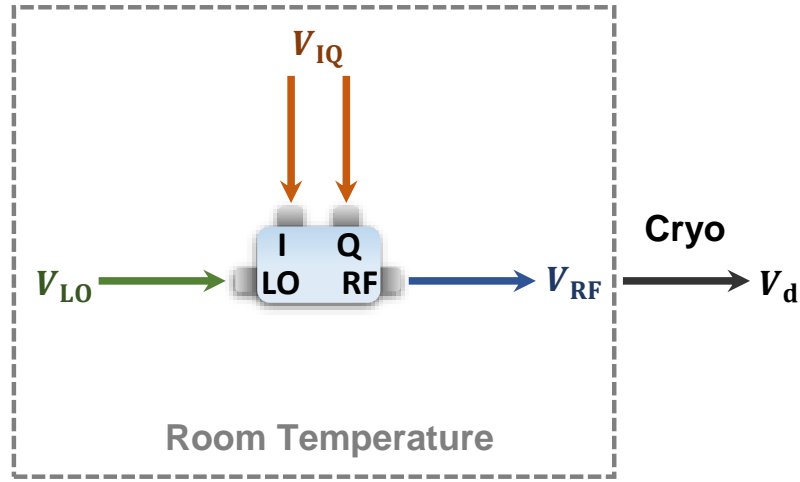


FIG. S5. **Generation of XY drive via frequency mixing.** The intrinsic local oscillation (LO) is generated from a microwave signal source, while the input IQ signals are generated from two channels of the arbitrary waveform generator. The whole circuit is mixed at room temperature and then goes into cryoelectronics (dilution refrigerator). If the amplitude of LO is fixed, the output pulse amplitude will be proportional to the amplitude of IQ signals in small amplitude cases where the IQ mixer is in a linear work region.

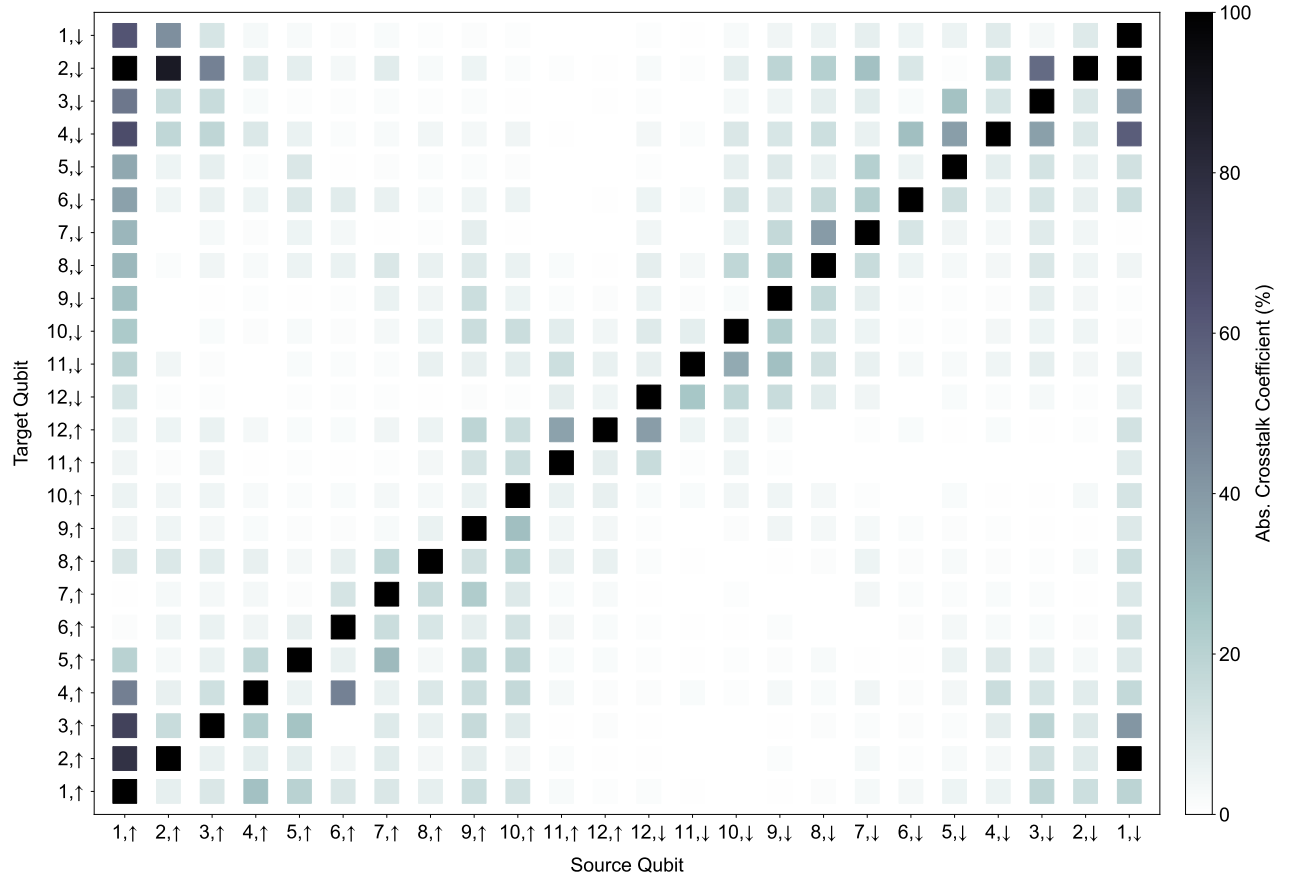


FIG. S6. **Partial crosstalk matrix of XY drive.** The heatmap represents the modulus of the crosstalk coefficient, namely $|c_{ij}|$. Here, we show the crosstalks between 24 qubits in the ladder.

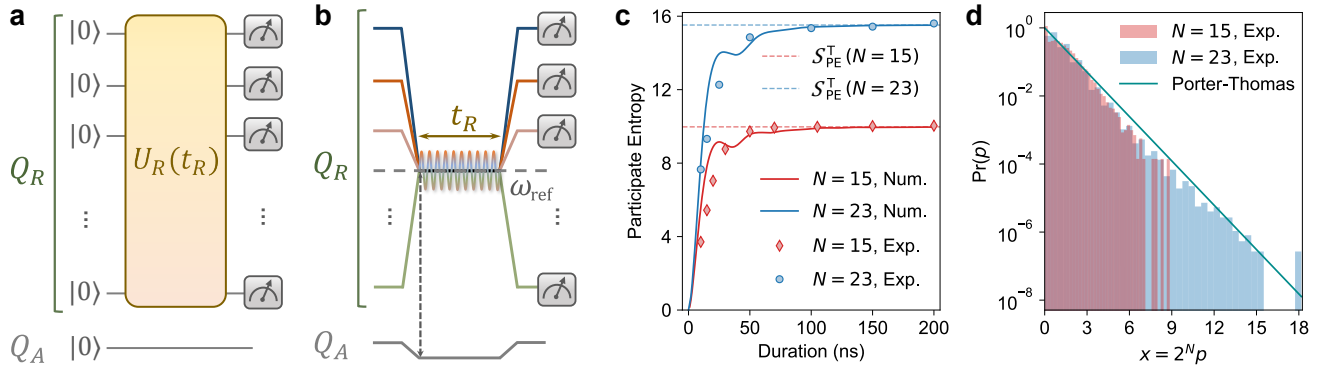


FIG. S7. **Generation and characterization of the XY drive approach to prepare the pseudo-random states.** **a**, The schematic diagram of the quantum circuit. **b**, The corresponding experimental pulse sequence. We bias the auxiliary qubit Q_A away from the resonance frequency and apply the XY drive pulses on all the remainder qubits Q_R participating in the resonance at frequency $\omega_{\text{ref}} \approx 4.534 \text{ GHz}$, with a duration t_R . **c**, The evolution of participate entropy S_{PE} vs. the duration of XY drive. The dashed line represents the participate entropy of N -qubit pseudo-random state. Here, we fix $Q_{1,\uparrow}$ as Q_A , and N is the total number of Q_R . **d**, The bitstring histogram of the measured $D = 2^N$ joint probabilities. The solid line shows the ideal results of Porter-Thomas distribution. For $N = 15$ and $N = 23$, we perform $N_s = 5 \times 10^5$ and $N_s = 3 \times 10^7$ single-shot measurements, respectively

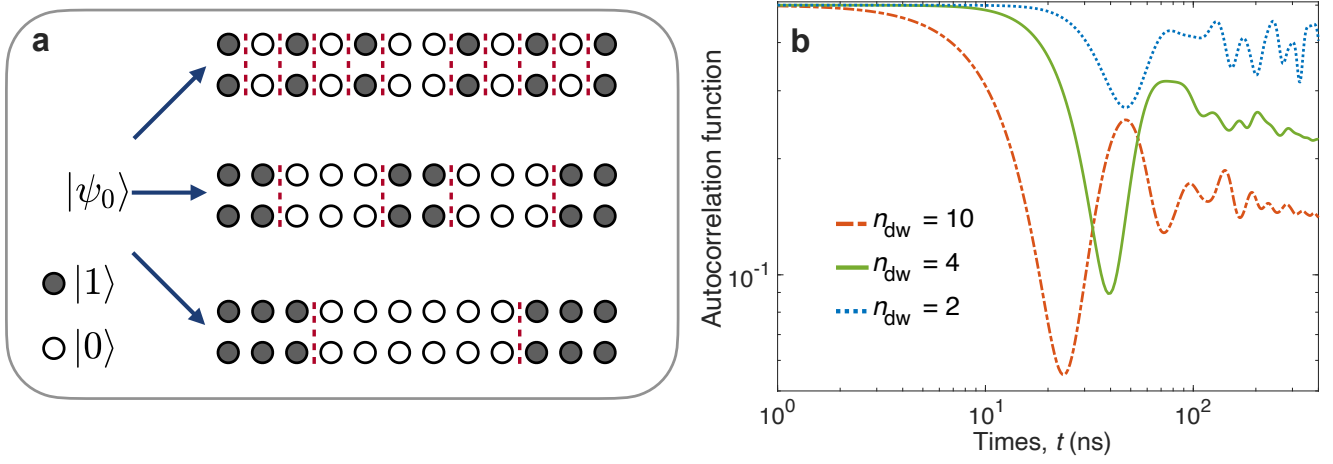


FIG. S8. **Additional numerical results for the spin transport on the titled superconducting qubit ladder.** **a**, Schematic diagram of three different product states $|\psi_0\rangle$ for the definition of the autocorrelation function $C_{1,1} = \langle \psi_0 | \hat{\rho}_1(t) \hat{\rho}_1 | \psi_0 \rangle$. From the top to bottom, the domain wall number of product states $|\psi_0\rangle$ is $n_{dw} = 10, 4$, and 2 , respectively. **b**, Time evolution of the autocorrelation function $C_{1,1} = \langle \psi_0 | \hat{\rho}_1(t) \hat{\rho}_1 | \psi_0 \rangle$ with the product states shown in **a** for the titled superconducting qubit ladder with $W_S/2\pi = 60$ MHz.

I. MODEL AND HAMILTONIAN

In this experiment, we use a ladder-type superconducting quantum processor with 30 programmable superconducting transmon qubits, which is identical to the device in ref. [52]. The optical micrograph and coupling strengths of the chip are shown in Fig. S1, and the device parameters are listed in Table S1. The Hamiltonian of the total system can be essentially described by a Bose-Hubbard model of a ladder

$$\hat{H}_{\text{BH}} = \sum_{i=1}^N h_i \hat{a}_i^\dagger \hat{a}_i - \frac{E_{C,j}}{2} \hat{a}_j^\dagger \hat{a}_j^\dagger \hat{a}_j \hat{a}_j + \hat{H}_I, \quad (\text{S1})$$

where N is the total number of qubits, \hat{a}^\dagger (\hat{a}) denotes the bosonic creation (annihilation) operator, h_j is the tunable on-site potential, $E_{C,j}$ denotes the on-site charge energy, representing the magnitude of anharmonicity, and \hat{H}_I is the Hamiltonian for the interactions between qubits. For qubits connected in a ladder-type with two coupled chains (' \uparrow ' and ' \downarrow '), the interaction Hamiltonian \hat{H}_I is mainly derived from the nearest-neighbor (NN) rung (vertical, ' \perp ') and intrachain (parallel, ' \parallel ') hopping couplings, namely

$$\hat{H}_\perp = \sum_{j=1}^L J_j^\perp (\hat{a}_{j,\uparrow}^\dagger \hat{a}_{j,\downarrow} + \text{H.c.}), \quad (\text{S2})$$

$$\hat{H}_\parallel = \sum_{m \in \{\uparrow, \downarrow\}} \sum_{j=1}^{L-1} J_{j,m}^\parallel (\hat{a}_{j,m}^\dagger \hat{a}_{j+1,m} + \text{H.c.}), \quad (\text{S3})$$

where $L = N/2$ is the length of each chain, J_j^\perp and $J_{j,m}^\parallel$ are the rung and intrachain coupling strengths. The mean values of $J_j^\perp/2\pi$ and $J_{j,m}^\parallel/2\pi$ are 6.562 MHz and 7.258 MHz, respectively. In addition, it is inevitable that small next-nearest-neighbor (NNN) interactions are present, including the hopping interactions between the diagonal qubits of the upper and lower chains (' \times ', diagonal down ' \searrow ' and diagonal up ' \swarrow ') and between NNN qubits on each chain (' \cap '), and the corresponding Hamiltonians are

$$\hat{H}_\times = \sum_{j=1}^{L-1} J_j^\searrow (\hat{a}_{j,\uparrow}^\dagger \hat{a}_{j+1,\downarrow} + \text{H.c.}) + J_j^\swarrow (\hat{a}_{j,\downarrow}^\dagger \hat{a}_{j+1,\uparrow} + \text{H.c.}), \quad (\text{S4})$$

$$\hat{H}_\cap = \sum_{m \in \{\uparrow, \downarrow\}} \sum_{j=1}^{L-2} J_{j,m}^\cap (\hat{a}_{j,m}^\dagger \hat{a}_{j+2,m} + \text{H.c.}), \quad (\text{S5})$$

where J_j^\searrow , J_j^\swarrow and $J_{j,m}^\cap$ are the strengths of diagonal down, diagonal up and parallel NNN hopping interactions, respectively. In short, for numerical simulations, we consider $\hat{H}_I = \hat{H}_\perp + \hat{H}_\parallel + \hat{H}_\times + \hat{H}_\cap$.

In our quantum processor, the anharmonicity (≥ 200 MHz) is much greater than the coupling interaction and the model can be viewed as a ladder-type lattice of hard-core bosons [52], i.e., the Eq. (1) in the main text. Our work aims to study the infinite-temperature spin transport in this model. To achieve this, we need to prepare the pseudo-random states. This supplementary focuses on the XY drive approach to generating the pseudo-random state of superconducting qubits. In Sec. III-V, we cover the details of calibrating XY drive and correcting the crosstalk. The generation and characterization of pseudo-random states are presented in Sec. VI. Additional numerical results are displayed in Sec. VII.

II. WIRING INFORMATION

The typical wiring information is shown in Fig. S2, in which from up to down are the control lines of qubit (XY and Z), readout, and Josephson parametric amplifier (JPA), respectively. From left to right, the ambient temperature decreases from room temperature to 12 mK in a BlueFors dilution refrigerator. We combine the high-frequency XY signal with the low-frequency Z bias by using directional couplers at room temperature. The XY signals are generated via frequency mixing. In detail, we use the IQ mixer to mix the intrinsic local oscillation (LO) from a microwave signal source and the IQ signals generated from two channels of arbitrary waveform generator (AWG). The output microwave signal is programmable, which depends on the pulses written into IQ signals. The joint readout signals are sent through the transmission line and amplified by the JPA, a cryo low-noise amplifier (LNA) and a room-temperature RF amplifier (RFA), and finally demodulated by the analog-digital converter (ADC).

III. LAGRANGIAN AND HAMILTONIAN OF SINGLE DRIVEN QUBIT

As shown in Fig. S3, when a time-dependent driving voltage $V_d(t)$ is added into a transmon qubit, the driving current I_d can be split into the qubit capacitance term I_C and the Josephson junction term I_J . Meanwhile, according to Kirchhoff voltage law, the total voltage reduction through either of the two branches must be zero. Thus, one can obtain the following motion equation

$$\begin{cases} I_d = I_C + I_J \\ -\dot{V}_d + \frac{I_d}{C_d} + \frac{I_C}{C} = 0 \\ -\dot{V}_d + \frac{I_d}{C_d} + L\ddot{\Phi} = 0 \end{cases} \Rightarrow \ddot{\Phi} + \frac{1}{C_\Sigma L} \Phi - \frac{C_d \dot{V}_d(t)}{C_\Sigma} = 0, \quad (\text{S6})$$

where $C_\Sigma = C + C_d$, $\Phi = LI_J$. Here C_d , C and L are the driving capacitance, qubit capacitance, and nonlinear inductance, respectively. The above equation can be viewed as the Euler-Lagrange equation $\frac{\partial \mathcal{L}_{\text{driven}}}{\partial \Phi} - \frac{d}{dt} \frac{\partial \mathcal{L}_{\text{driven}}}{\partial \dot{\Phi}} = 0$, where the Lagrangian of this driven qubit can be constructed as

$$\mathcal{L}_{\text{driven}} = \frac{1}{2} C \dot{\Phi}^2 + \frac{1}{2} C_d \left(V_d(t) - \dot{\Phi} \right)^2 - \frac{\Phi^2}{2L}, \quad (\text{S7})$$

where C_d is the driving capacitance. In Eq. S7, the first term represents the charge energy of C , the second term denotes the charge energy of C_d caused by induced electromotive force, and the last term is the inductance energy of L .

IV. TWO COUPLED DRIVEN QUBITS

Now we consider two driven qubits Q_i and Q_j in the circuit (see Fig. S4). The total Lagrangian can be expressed as

$$\mathcal{L}_{\text{driven}}^{(i,j)} = \sum_{q=i,j} \left(\frac{1}{2} C_q \dot{\Phi}_q^2 - \frac{\Phi_q^2}{2L_q} \right) + \frac{1}{2} C_{d,i} \left(V_{d,i}(t) - \dot{\Phi}_i \right)^2 + \frac{1}{2} C_{d,j} \left(V_{d,j}(t) - \dot{\Phi}_j \right)^2 + \frac{1}{2} C_{ij} \left(\dot{\Phi}_j - \dot{\Phi}_i \right)^2, \quad (\text{S8})$$

where C_{ij} is the coupling capacitance. The corresponding canonical momentums are

$$\begin{bmatrix} \tilde{Q}_i \\ \tilde{Q}_j \end{bmatrix} = \begin{bmatrix} \frac{\partial \mathcal{L}_{\text{driven}}^{(i,j)}}{\partial \dot{\Phi}_i} \\ \frac{\partial \mathcal{L}_{\text{driven}}^{(i,j)}}{\partial \dot{\Phi}_j} \end{bmatrix} = \begin{bmatrix} C_{\Sigma_i} + C_{ij} & -C_{ij} \\ -C_{ij} & C_{\Sigma_j} + C_{ij} \end{bmatrix} \begin{bmatrix} \dot{\Phi}_i \\ \dot{\Phi}_j \end{bmatrix} - \begin{bmatrix} C_{d,i} V_{d,i} \\ C_{d,j} V_{d,j} \end{bmatrix}, \quad (\text{S9})$$

where $C_{\Sigma_i} = C_i + C_{d,i}$ and $C_{\Sigma_j} = C_j + C_{d,j}$, and thus

$$\begin{bmatrix} \dot{\Phi}_i \\ \dot{\Phi}_j \end{bmatrix} = \frac{1}{\|\mathbf{C}\|} \begin{bmatrix} C_{\Sigma_j} + C_{ij} & C_{ij} \\ C_{ij} & C_{\Sigma_i} + C_{ij} \end{bmatrix} \begin{bmatrix} \tilde{Q}_i + C_{d,i} V_{d,i} \\ \tilde{Q}_j + C_{d,j} V_{d,j} \end{bmatrix}, \quad (\text{S10})$$

where $\|\mathbf{C}\| = C_{\Sigma_i} C_{\Sigma_j} + C_{\Sigma_i} C_{ij} + C_{\Sigma_j} C_{ij}$ is the determinant of the capacitance matrix $\mathbf{C} = \begin{bmatrix} C_{\Sigma_i} + C_{ij} & -C_{ij} \\ -C_{ij} & C_{\Sigma_j} + C_{ij} \end{bmatrix}$. Substituting Eq. (S10) into Eq. (S8), we obtain

$$\mathcal{L}_{\text{driven}}^{(i,j)} = \frac{\tilde{Q}_i^2}{2\tilde{C}_{\Sigma_i}} + \frac{\tilde{Q}_j^2}{2\tilde{C}_{\Sigma_j}} + \frac{\tilde{Q}_i \tilde{Q}_j}{\tilde{C}_{ij}}, \quad (\text{S11})$$

with the effective capacitance parameters

$$\tilde{C}_{\Sigma_i} = C_{\Sigma_i} + (C_{\Sigma_j} \| C_{ij}) = C_{\Sigma_i} + \frac{C_{\Sigma_j} C_{ij}}{C_{\Sigma_j} + C_{ij}}, \quad (\text{S12})$$

$$\tilde{C}_{\Sigma_j} = C_{\Sigma_j} + (C_{\Sigma_i} \| C_{ij}) = C_{\Sigma_j} + \frac{C_{\Sigma_i} C_{ij}}{C_{\Sigma_i} + C_{ij}}, \quad (\text{S13})$$

$$\tilde{C}_{ij} = \frac{C_{\Sigma_i} C_{ij} + C_{\Sigma_j} C_{ij} + C_{\Sigma_i} C_{\Sigma_j}}{C_{ij}}. \quad (\text{S14})$$

Then the total Hamiltonian is given by the Legendre transformation:

$$\begin{aligned} H_{\text{driven}}^{(i,j)} &= \tilde{Q}_i \dot{\Phi}_i + \tilde{Q}_j \dot{\Phi}_j - \mathcal{L}_{\text{driven}}^{(i,j)} \\ &= \sum_{q=i,j} \left(\frac{\tilde{Q}_q^2}{2\tilde{C}_{\Sigma_q}} + \frac{\Phi_q^2}{2L_q} \right) + \frac{\tilde{Q}_i \tilde{Q}_j}{\tilde{C}_{ij}} + \left(\frac{C_{d,i}}{\tilde{C}_{\Sigma_i}} V_{d,i}(t) + \frac{C_{d,j}}{\tilde{C}_{\Sigma_j}} V_{d,j}(t) \right) \tilde{Q}_i + \left(\frac{C_{d,j}}{\tilde{C}_{\Sigma_j}} V_{d,j}(t) + \frac{C_{d,i}}{\tilde{C}_{\Sigma_i}} V_{d,i}(t) \right) \tilde{Q}_j. \end{aligned} \quad (\text{S15})$$

Using canonical quantization, we introduce

$$\begin{cases} \hat{\tilde{Q}}_q = i\tilde{Q}_{\text{zpf},q}(\hat{a}_q^\dagger - \hat{a}_q) \\ \hat{\tilde{\Phi}}_q = \Phi_{\text{zpf},q}(\hat{a}_q^\dagger + \hat{a}_q) \end{cases} \quad (\text{S16})$$

with $q \in \{i, j\}$, $\tilde{Q}_{\text{zpf},q} = \sqrt{\hbar(\tilde{C}_{\Sigma_q}/L_{c,q})^{1/2}/2}$ and $\Phi_{\text{zpf},q} = \sqrt{\hbar(L_{c,q}/\tilde{C}_{\Sigma_q})^{1/2}/2}$. The quantized Hamiltonian thus is

$$\hat{H}_{\text{driven}}^{(i,j)} = \hat{H}_{\text{driven}}^{(i)} + \hat{H}_{\text{driven}}^{(j)} + \hat{H}_{\text{int}}^{(i,j)}, \quad (\text{S17})$$

$$\hat{H}_{\text{driven}}^{(q)} = \hbar\omega_q\hat{a}_q^\dagger\hat{a}_q - \frac{E_{C_q}}{2}\hat{a}_q^\dagger\hat{a}_q^\dagger\hat{a}_q\hat{a}_q + i\hbar\tilde{\Omega}_q(t)(\hat{a}_q^\dagger - \hat{a}_q), \quad q \in \{i, j\}, \quad (\text{S18})$$

$$\hat{H}_{\text{int}}^{(i,j)} = \hbar J_{i,j}(\hat{a}_i^\dagger - \hat{a}_i)(\hat{a}_j - \hat{a}_j^\dagger), \quad (\text{S19})$$

where the parameters are

$$\hbar\omega_q = \sqrt{8E_{C_q}E_{J_q}} - E_{C_q}, \quad E_{C_q} = \frac{e^2}{2\tilde{C}_q}, \quad E_{J_q} = \frac{\Phi_0^2}{4\pi^2 L_{c,q}}, \quad (\text{S20})$$

$$J_{i,j} = \frac{\tilde{Q}_{\text{zpf},i}\tilde{Q}_{\text{zpf},j}}{\hbar\tilde{C}_{ij}} = \frac{\sqrt{\tilde{C}_{\Sigma_i}\tilde{C}_{\Sigma_j}}}{2\tilde{C}_{ij}} \sqrt{\left(\omega_i + \frac{E_{C_i}}{\hbar}\right)\left(\omega_j + \frac{E_{C_j}}{\hbar}\right)} \approx \frac{C_{ij}\sqrt{\omega_i\omega_j}}{2\sqrt{(C_{\Sigma_i} + C_{ij})(C_{\Sigma_j} + C_{ij})}}, \quad (\text{S21})$$

$$\tilde{\Omega}_i(t) = \epsilon_{ii}\left(V_{d,i}(t) + \frac{\epsilon_{ij}}{\epsilon_{ii}}V_{d,j}(t)\right), \quad \tilde{\Omega}_j(t) = \epsilon_{jj}\left(V_{d,j}(t) + \frac{\epsilon_{ji}}{\epsilon_{jj}}V_{d,i}(t)\right), \quad (\text{S22})$$

$$\epsilon_{ii} = \frac{\tilde{Q}_{\text{zpf},i}C_{d,i}}{\hbar\tilde{C}_{\Sigma_i}}, \quad \epsilon_{ij} = \frac{\tilde{Q}_{\text{zpf},i}C_{d,j}}{\hbar\tilde{C}_{ij}}, \quad \epsilon_{jj} = \frac{\tilde{Q}_{\text{zpf},j}C_{d,j}}{\hbar\tilde{C}_{\Sigma_j}}, \quad \epsilon_{ji} = \frac{\tilde{Q}_{\text{zpf},j}C_{d,i}}{\hbar\tilde{C}_{ij}}. \quad (\text{S23})$$

Focusing on Eqs. (S18), (S22) and (S23), one can notice that the local driving Hamiltonian of each qubit depends on both external drive $V_{d,i}(t)$ and $V_{d,j}(t)$ due to the presence of coupling capacitance. However, this crosstalk is usually very small. As an example, we take the typical values $C_{d,i} = C_{d,j} = 30$ aF, $C_i = C_j = 85$ fF and $C_{ij} = 0.25$ fF. Then we have $\epsilon_{ij}/\epsilon_{ii} = \epsilon_{ji}/\epsilon_{jj} \approx 0.3\%$, suggesting a low level of this crosstalk. In fact, most of the crosstalk comes from the classical microwave crosstalk. The total crosstalk is the sum of the classical microwave crosstalk and the crosstalk due to the coupling capacitance, as explained in Methods of the main text.

V. GENERATION OF XY DRIVE PULSE

As shown in Fig. S5, we generate XY drive pulse by using IQ mixer. The output driving pulse results from mixing the IQ signals with a intrinsic LO (Fig. S5). Although Ω is proportional to the actual driving amplitude V_d , the relationship between Ω and the input amplitude of IQ signals V_{IQ} is not always linear due to the semiconductor nature of the IQ mixer (GaAs and similar semiconductor materials). When V_{IQ} is relatively small, IQ mixer is in the linear work region and $V_d \propto V_{\text{IQ}}$ satisfies. However, the strong amplitude leads to a nonlinear relationship between V_d and V_{IQ} , so that $\Omega \propto V_{\text{IQ}}$ is not valid in the saturation region. This may be caused by the velocity saturation of carriers in the IQ mixer. In order to analytically describe Ω versus V_{IQ} , we impose the following smooth piecewise function and its inverse:

$$\Omega = \begin{cases} \eta V_{\text{IQ}}, & (V_{\text{IQ}} \leq V_{\text{IQ}}^{\text{sat}}) \\ \Omega_{\text{max}} - (\Omega_{\text{max}} - \eta V_{\text{IQ}}^{\text{sat}}) e^{-\frac{\eta(V_{\text{IQ}} - V_{\text{IQ}}^{\text{sat}})}{\Omega_{\text{max}} - \eta V_{\text{IQ}}^{\text{sat}}}}, & (V_{\text{IQ}} > V_{\text{IQ}}^{\text{sat}}) \end{cases} \quad (\text{S24})$$

$$V_{\text{IQ}} = \begin{cases} \frac{1}{\eta}\Omega, & (\Omega \leq \eta V_{\text{IQ}}^{\text{sat}}) \\ V_{\text{IQ}}^{\text{sat}} + \left(\frac{\Omega_{\text{max}}}{\eta} - V_{\text{IQ}}^{\text{sat}}\right) \ln\left(\frac{\Omega_{\text{max}} - \eta V_{\text{IQ}}^{\text{sat}}}{\Omega_{\text{max}} - \Omega}\right), & (\Omega > \eta V_{\text{IQ}}^{\text{sat}}) \end{cases} \quad (\text{S25})$$

where η , $V_{\text{IQ}}^{\text{sat}}$ and Ω_{max} are the parameters to be fitted. Here η is the slope in linear region that represents the Rabi frequency corresponding to the unit amplitude of XY driving (IQ signals), $V_{\text{IQ}}^{\text{sat}}$ denotes the critical amplitude before entering the saturation region of IQ mixer, and Ω_{max} is the maximum Rabi frequency when $V_{\text{IQ}} \rightarrow \infty$.

Note that it is convenient to use the linear region of IQ mixer. In this case, the relationship between Rabi frequency and the input IQ signals can be expressed as $\mathbf{V}_{\text{IQ}} = \boldsymbol{\eta}\boldsymbol{\Omega}$, where $\boldsymbol{\eta} = \text{diag}\{\eta_1, \eta_2, \dots, \eta_N\}$, $\mathbf{V}_{\text{IQ}} = [V_{\text{IQ},1}, V_{\text{IQ},2}, \dots, V_{\text{IQ},N}]^T$ and $\boldsymbol{\Omega} = [\Omega_1, \Omega_2, \dots, \Omega_N]^T$. Thus, the crosstalk matrix of IQ signals is given by $\mathbf{M}_{\text{V}_{\text{IQ}}} = \boldsymbol{\eta}\mathbf{M}_{\boldsymbol{\Omega}}\boldsymbol{\eta}^{-1}$, where $\boldsymbol{\eta}$ can be measured by the vacuum Rabi experiments, and the measurement of $\mathbf{M}_{\boldsymbol{\Omega}}$ is mentioned in the main text. Here we show the partial crosstalk matrix between the 24 qubits used in experiments in Fig. S6.

VI. XY DRIVE APPROACH TO PSEUDO-RANDOM STATES

For the pseudo-random state $|\psi^R\rangle$, we can define the probability with respect to the computational basis $|k\rangle$ as $p_k = |\langle k|\psi^R\rangle|^2$. It has been shown that the distribution of the probabilities $\{p = p_k\}$ will approximate the so-called Porter-Thomas distribution [31-33]

$$\Pr(p) = D e^{-Dp}, \quad (\text{S26})$$

where $D = 2^N$ is the total dimension of the Hilbert space. To generate the pseudo-random states via the evolution \hat{U}_R in this experiment (seen in the main text or Fig. S7a), we bias the auxiliary qubit Q_A away from the resonance frequency and apply the XY drive pulses on all the remainder qubits Q_R participating in the resonance. The experimental pulse diagram is shown in Fig. S7b. After a time t_R , we perform joint readout of Q_R with N_s single-shot measurements to obtain the joint probabilities, and then calculate the participate entropy

$$S_{\text{PE}}(t_R) = - \sum_{k=1}^D p_k(t_R) \ln p_k(t_R), \quad (\text{S27})$$

where p_n is the joint probabilities of all $D = 2^N$ bitstrings. As shown in Fig. S7c, the participate entropy increases rapidly and then tends to a stable value. This value matches the participate entropy of the pseudo-random state, namely

$$S_{\text{PE},|\psi^R\rangle} = -D \int_0^\infty dp \Pr(p) p \ln p = \ln D - 1 + \gamma, \quad (\text{S28})$$

where $\gamma \approx 0.577$ is the Euler constant. The final state after a long-time evolution is therefore closer to a pseudo-random state, which shows the Porter-Thomas distribution of the bitstring joint probabilities in the statistical histogram, see Fig. S7d. In the experiment, we select $t_R = 200$ ns to generate the pseudo-random state and use this state as the initial state for subsequent interactions.

VII. ADDITIONAL NUMERICS AND DISCUSSIONS

In this section, we numerically study another type of autocorrelation functions which are defined by the average over a product state $|\psi_0\rangle$. In the main text, we focus on the infinite-temperature autocorrelation function $C_{\mathbf{r},\mathbf{r}} = \text{Tr}[\hat{\rho}_{\mathbf{r}}(t)\hat{\rho}_{\mathbf{r}}]/D$ with D being the dimension of the Hilbert space. Alternatively, one can also consider the autocorrelation function average over a product state $|\psi_0\rangle$, i.e.,

$$C_{\mathbf{r},\mathbf{r}}(|\psi_0\rangle) = \langle \psi_0 | \hat{\rho}_{\mathbf{r}}(t) \hat{\rho}_{\mathbf{r}} | \psi_0 \rangle. \quad (\text{S29})$$

Here, we reveal that the autocorrelation function $C_{\mathbf{r},\mathbf{r}}(|\psi_0\rangle)$ cannot show generic properties of spin transport, and the dynamics of $C_{\mathbf{r},\mathbf{r}}(|\psi_0\rangle)$ is highly dependent on the choice of $|\psi_0\rangle$.

We consider the titled superconducting qubit ladder consisting of 24 qubits with $W_S/2\pi = 60$ MHz, and the slope of the linear potential $\gamma/2\pi \simeq 11$ MHz. Three chosen product states $|\psi_0\rangle$ for the autocorrelation function (S29) are shown in Fig. S8a. The product states with the domain wall number $n_{\text{dw}} = 10, 4$, and 2 are labeled as $|\psi_0^{(10)}\rangle$, $|\psi_0^{(4)}\rangle$, and $|\psi_0^{(2)}\rangle$, respectively. It can be directly calculated that the $\langle \psi_0^{(10)} | \hat{H} | \psi_0^{(10)} \rangle = \langle \psi_0^{(4)} | \hat{H} | \psi_0^{(4)} \rangle = \langle \psi_0^{(2)} | \hat{H} | \psi_0^{(2)} \rangle$. The results of the time evolution of $C_{\mathbf{r},\mathbf{r}}(|\psi_0\rangle)$ with $\mathbf{r} = 1$ are presented in Fig. S8b. It is seen that for the product state with $n_{\text{dw}} = 2$, the decay of $C_{\mathbf{r},\mathbf{r}}(|\psi_0\rangle)$ can be neglected, while the decay becomes stronger when we consider $C_{\mathbf{r},\mathbf{r}}(|\psi_0\rangle)$ with $n_{\text{dw}} = 4$ and 10 .

Actually, in ref. [15], it has been shown that the infinite-temperature autocorrelation function can be expanded as

$$C_{\mathbf{r},\mathbf{r}} = \frac{1}{D} \text{Tr}[\hat{\rho}_{\mathbf{r}}(t)\hat{\rho}_{\mathbf{r}}] = \frac{1}{D} \sum_{k=1}^D \langle k | \hat{\rho}_{\mathbf{r}}(t) \hat{\rho}_{\mathbf{r}} | k \rangle, \quad (\text{S30})$$

where $|k\rangle = |\sigma_{1,\uparrow}\sigma_{2,\uparrow}\dots\sigma_{12,\uparrow}; \sigma_{1,\downarrow}\sigma_{2,\downarrow}\dots\sigma_{12,\downarrow}\rangle$ is the product states in the σ^z basis. As shown in Fig. S8b, a single term $\langle k | \hat{\rho}_{\mathbf{r}}(t) \hat{\rho}_{\mathbf{r}} | k \rangle$ in (S30) cannot capture the properties of infinite-temperature spin transport. In our work, we employ the quantum circuit shown in Fig. 1c to directly measure the infinite-temperature autocorrelation function, without the need of sampling different product states.